Redox Biology 50 (2022) 102257

Contents lists available at ScienceDirect

Redox Biology

journal homepage: www.elsevier.com/locate/redox

T lymphocyte-derived extracellular vesicles aggravate abdominal aortic aneurysm by promoting macrophage lipid peroxidation and migration via pyruvate kinase muscle isozyme 2

Guohui Dang [a,1], Tianrun Li [b,1], Dongmin Yang [a], Guangxin Yang [b], Xing Du [a], Juan Yang [a], Yutong Miao [a], Lulu Han [a], Xiaolong Ma [a], Yuwei Song [a], Bo Liu [a], Xuan Li [b], Xian Wang [a], Juan Feng [a,b,c,*]

[a] *Department of Physiology and Pathophysiology, School of Basic Medical Sciences, Key Laboratory of Molecular Cardiovascular Science, Ministry of Education, Peking University, 38 Xueyuan Road, Haidian District, Beijing 100191, China*

[b] *Department of Interventional Radiology and Vascular Surgery, Peking University Third Hospital, North Garden Road 49, Haidian District, Beijing 100191, China*

[c] *Department of Integration of Chinese and Western Medicine, School of Basic Medical Sciences, Peking University, 38 Xueyuan Road, Haidian District, Beijing 100191, China*

ARTICLE INFO

Keywords:
Pyruvate kinase muscle isozyme 2
Abdominal aortic aneurysm
Extracellular vesicles
Macrophage migration
Lipid peroxidation

ABSTRACT

T lymphocyte and macrophage infiltration in the aortic wall is critical for abdominal aortic aneurysm (AAA). However, how T lymphocytes interact with macrophages in the pathogenesis of AAA remains largely uncharacterized. In an elastase-induced murine AAA model, we first found that the expression of pyruvate kinase muscle isozyme 2 (PKM2), the last rate-limiting enzyme in glycolysis, was increased in infiltrated T lymphocytes of vascular lesions. T lymphocyte-specific PKM2 deficiency in mice (LckCrePKM2$^{fl/fl}$) or intraperitoneal administration of the sphingomyelinase inhibitor GW4869 caused a significant attenuation of the elastase-increased aortic diameter, AAA incidence, elastic fiber disruption, matrix metalloproteinases (MMPs) expression, and macrophage infiltration in the vascular adventitia compared with those in PKM2$^{fl/fl}$ mice. Mechanistically, extracellular vesicles (EVs) derived from PKM2-activated T lymphocytes elevated macrophage iron accumulation, lipid peroxidation, and migration *in vitro*, while macrophages treated with EVs from PKM2-null T lymphocytes or pretreated with the lipid peroxidation inhibitors ferrostatin-1 (Fer-1), liproxstatin-1 (Lip-1), or the iron chelating agent deferoxamine mesylate (DFOM) reversed these effects. In vascular lesions of elastase-induced LckCrePKM2$^{fl/fl}$ mice with AAA, the oxidant system weakened, with downregulated 4-hydroxynonenal (4-HNE) levels and strengthened antioxidant defense systems with upregulated glutathione peroxidase 4 (GPX4) and cystine/glutamate antiporter solute carrier family 7 member 11 (Slc7a11) expressions in macrophages. High-throughput metabolomics showed that EVs derived from PKM2-activated T lymphocytes contained increased levels of polyunsaturated fatty acid (PUFA)-containing phospholipids, which may provide abundant substrates for lipid peroxidation in target macrophages. More importantly, upregulated T lymphocyte PKM2 expression was also found in clinical AAA subjects, and EVs isolated from AAA patient plasma enhanced macrophage iron accumulation, lipid peroxidation, and migration *ex vivo*. Therefore, from cell-cell crosstalk and metabolic perspectives, the present study shows that PKM2-activated T lymphocyte-derived EVs may drive AAA progression by promoting macrophage redox imbalance and migration, and targeting the T lymphocyte-EV-macrophage axis may be a potential strategy for early warning and treating AAA.

1. Introduction

Abdominal aortic aneurysm (AAA) is a progressive segmental

* Corresponding author. Department of Physiology and Pathophysiology, School of Basic Medical Sciences, Key Laboratory of Molecular Cardiovascular Science, Ministry of Education, Peking University, Beijing, 100191, PR China.
E-mail address: juanfeng@bjmu.edu.cn (J. Feng).
[1] These authors contributed equally to this article.

https://doi.org/10.1016/j.redox.2022.102257
Received 16 December 2021; Received in revised form 22 January 2022; Accepted 31 January 2022
Available online 4 February 2022

Abbreviations

AAA	abdominal aortic aneurysm
PKM2	pyruvate kinase muscle isozyme 2
MMP	matrix metalloproteinase
EVs	extracellular vesicles
Fer-1	ferrostatin-1
Lip-1	liproxstatin-1
DFOM	deferoxamine mesylate
4-HNE	4-hydroxynonenal
GPX4	glutathione peroxidase 4
Slc7a11	solute carrier family 7 member 11
PL	phospholipids
PUFA	polyunsaturated fatty acids
KLF5	Krüppel-like factor 5
ROS	reactive oxygen species
MSC	mesenchymal stromal cell
CTA	computed tomography angiography
LPO	lipid peroxidation
MDA	malondialdehyde
Hcy	homocysteine
GSH	glutathione
Ptgs2	prostaglandin endoperoxidase synthase 2
SOD-1	superoxide dismutase 1
Cat	catalase
PC	phosphatidylcholine
PE	phosphatidylethanolamine
PBMC	peripheral blood mononuclear cell

dilation of the abdominal aorta, is associated with high mortality, and is always accompanied by inflammatory responses in the wall of the abdominal aorta [1]. In addition to the vascular endothelium, the contribution of the adventitial inflammatory immune microenvironment to vascular remodeling has received increasing attention. Based on recent scRNA-seq data, macrophages account for the largest proportion of infiltrating immune cells in elastase-induced AAA, and most of them are derived from circulating monocytes and then promote the occurrence of AAA [2]. Although distinct chemokines or cytokines and ECM degradation products promote the recruitment and activation of immune cells to the aortic wall, the potential mechanisms of macrophage migration still need further investigation.

The current strategies that reduce macrophages in the aneurysm wall to attenuate AAA in mice are mainly focused on macrophage depletion [3] or cytokine inhibition [4]. Deciphering the intracellular molecular mechanisms by which macrophages themselves regulate their migratory ability will provide new attitudes and potential intervention strategies. Recent research showed that Krüppel-like factor 5 (KLF5)-dependent regulation of Myo9b/RhoA is required for podosome formation and macrophage migration during AAA formation [5]. In macrophages, reactive oxygen species (ROS) act as upstream regulators of RhoA and cytoskeletal organization, leading to impaired cell migration [6,7]. Macrophage ROS generation was demonstrated to markedly increase in aortic aneurysmal tissues [8]. Under oxidative stress, polyunsaturated fatty acid (PUFA)-containing phospholipids and cholesterol esters in the cellular membrane and lipoproteins can be readily oxidized to form a complex mixture of oxidation products [9]. The association of serum lipid peroxidation products with disease severity in AAA patients has been determined [10]. Additionally, iron is involved in the pathophysiology of AAA through oxidative stress [11], and the presence of lipids and iron-containing deposits in macrophages was confirmed in the human aneurysmal aortic wall [12]. Iron-dependent lipid radicals regulate cell migration in podocytes [13] and cancer cells [14], although there are many discrepancies. However, it remains unknown whether oxidative stress is directly involved in macrophage migration during AAA development, and if so, the types and exact roles of the oxidative stress products in cell motility need to be clarified.

Normally, inflammation in the aortic wall can be mediated by crosstalk among various cells. Extracellular vesicles (EVs), comprising exosomes and microvesicles, are now considered an additional mechanism for intercellular communication [15] and have been reported in multiple physiological and pathological processes [16,17]. Macrophage-derived EVs trigger matrix metallopeptidase 2 (MMP2) expression in vascular smooth muscle cells *in vitro* and then aggravate the progression of $CaPO_4$-induced AAA [18]. Human mesenchymal stromal cell (MSC)-derived EVs inhibit AAA formation in an elastase-treated mouse model by attenuating aortic inflammation and macrophage activation [19]. Although the potential mediator needs to be explored, it has been shown that monocytes mobilize from the spleen and give rise to abdominal aortic macrophages in response to Ang II, which is dependent on the presence of B lymphocytes [20]. This result indicates that the crosstalk among different immune cells, especially between monocytes and lymphocytes, can contribute to monocyte/macrophage migration and AAA development. In addition, T lymphocytes are another major leukocyte subset in human AAA, and T lymphocyte infiltration is strongly related to AAA size [21]. During elastase-induced AAA progression, T lymphocytes expand from 3.5% to 10.8% of total cells, whereas B lymphocytes do not increase and represent only 2.36% of the total cells [2]. A small portion of exosomes overlap with T lymphocyte markers in the adventitia of aneurysms; however, their exact role is not yet known [18]. Previously, we reported that T lymphocyte-derived EVs increase B lymphocyte pathogenic IgG production to facilitate murine vascular inflammation and atherogenesis [22]. Therefore, we will investigate whether EV-mediated T lymphocyte-macrophage interactions are involved in the pathogenesis of aneurysm development and the potential mechanisms in the present study.

Dysregulation of glucose metabolism is widely observed during various disorders [23,24]. Enhanced glycolytic activity and increased expression of the glucose transporters Glut1 and Glut3 have been observed in aneurysmal aortic walls. Glycolysis restriction significantly attenuates the dilatation of the abdominal aorta by inhibiting macrophage survival/proliferation and adherence to the endothelium, matrix metalloproteinase abundance and activity, and macrophage-mediated inflammatory cytokine production [25]. However, it is still unknown what cell type is a possible contributor to local vessel glucose-related disorders in AAA. The underlying molecular mechanisms other than glucose transport have not been determined. Pyruvate kinase muscle isozyme 2 (PKM2) is universally expressed and catalyzes the last and physiologically irreversible step in glycolysis. We have reported that homocysteine (Hcy) increases PKM2 protein expression and activity and mediates glycolysis-associated metabolic reprogramming in activated T lymphocytes, and targeting PKM2 may be a promising therapeutic strategy for hyperhomocysteinemia (HHcy)-accelatared atherosclerosis by inhibiting T and B lymphocyte activation via EV-dependent mechanisms [22,26]. Additionally, HHcy is closely related to AAA by exaggerating adventitial inflammation, in which mitochondrial ROS-mediated macrophage inflammasome activation and L-1β production play a pivotal role [27]. By using T lymphocyte PKM2-specific knockout mice and applying Hcy as a potential PKM2 activator, we will further explore whether T lymphocyte PKM2 is regulated by AAA and possible mediating mechanisms.

In this study, we revealed that EVs from PKM2-activated T lymphocytes can be taken up by recipient macrophages and then promote iron accumulation and lipid peroxidation in macrophages, consequently increasing their migration to promote murine AAA progression, which

was partly confirmed in clinical samples of AAA subjects. Therefore, targeting T-lymphocyte PKM2-EV-macrophage iron accumulation or the lipid peroxidation axis may be a novel potential strategy to treat macrophage-associated inflammation and AAA.

2. Materials and methods

2.1. Animal treatments

Mice were housed in the Animal Center of Peking University Health Science Center. LckCrePKM2$^{fl/fl}$ mice were generated by crossing PKM2$^{fl/fl}$ mice (24048, on a B6129SF1/J background) and Lck-Cre transgenic mice (Jax-003803) in our laboratory. For generation of a murine AAA model, 10-week-old male C57BL/6J mice were treated with elastase, as male mice are more susceptible to AAA than female mice. In brief, the mice were anaesthetized, and infrarenal abdominal aortas were exposed, isolated, and wrapped with sterile cotton soaked with 40 μL of elastase (E1250, Sigma-Aldrich, St. Louis, MO, USA) or saline (to serve as the sham group) for 40 min. Then, the elastase-soaked cotton was removed, and the abdominal cavities were washed with 0.9% saline twice before suturing the surgical incision. For the AAA model pretreated with GW4869 (D1692, Sigma-Aldrich, St. Louis, MO, USA), an inhibitor of sphingomyelinase, 9-week-old wild-type male C57BL/6J mice were randomly assigned to three groups: sham, AAA + GW4869, and AAA + vehicle. The mice were injected intraperitoneally once daily with GW4869 (1.25 mg/kg body weight) 7 days prior to elastase-induced AAA for a total of 21 daily injections (AAA + GW4869). GW4869 was dissolved in saline with 2.5% dimethylsulfoxide. The mice received injections of saline with 2.5% dimethylsulfoxide to a comparable volume for the AAA + vehicle group. All animal care and experimental procedures were reviewed and approved by the Institutional Animal Care and Use Committee of Peking University Health Science Center and complied with the U.S. Department of Agriculture, International Association for the Assessment and Accreditation of Laboratory Animal Care, and the National Institutes of Health Guide for the Care and Use of Laboratory Animals (NIH Publications No. 8023, revised 1978).

2.2. Participants

AAA patients chosen in this study were candidates for endovascular repair surgery at the Peking University Third Hospital. Patients with AAA were selected according to their aortic diameter, which was measured by computed tomography angiography (CTA) (aortic diameter>30 mm [28]; n = 7), and the control group included patients without symptoms or signs of AAA (n = 8). A total of 15 patients were approached by the vascular surgery staff, and they all agreed to provide informed consent. All participants are chosen randomly. This study was approved by the Peking University Hospital Biomedical Research Ethics Committee and in accordance with The Code of Ethics of the World Medical Association (Declaration of Helsinki) for experiments involving humans.

2.3. Cell isolation and culture

Splenic T lymphocytes were isolated from mice and purified by positive immunomagnetic cell sorting with magnetic microbeads against CD3 according to the manufacturer's protocol (130-094-973, Miltenyi Biotec, Bergisch Gladbach, Germany). Purified T lymphocytes were cultured in Roswell Park Memorial Institute (RPMI) 1640 medium (c11875500BT, Thermo Fisher Scientific, Waltham, MA, USA) supplemented with 10% (v/v) fetal bovine serum (900–108; Gemini Bio-Products, Sacramento, CA, USA) and 100 nM penicillin/streptomycin (Gibco, Gaithersburg, MD, USA) and maintained with anti-CD3 antibody (as basic stimulation for T lymphocytes, 1 μg/mL, 53057, BD Biosciences, San Jose, CA, USA).

Peritoneal macrophages were isolated from 8-week-old male wild-type C57BL/6J mice. The mouse abdomen was cleaned with 75% ethanol, the abdominal skin was removed to expose the peritoneum under sterile conditions, and then, 5 mL of PBS with 10% FBS was carefully injected into the peritoneal cavity. The mouse abdomen was gently massaged for 10 min. As much PBS as possible was slowly collected and then centrifuged for 10 min at 4 °C at 300 g to pellet the cells. Then, these cells were plated in complete RPMI medium with 10% (v/v) FBS and penicillin/streptomycin to allow macrophages to attach for 2 h. The medium was removed, adherent cells were washed with PBS, and new medium was added.

RAW264.7 cells, a mouse macrophage cell line (purchased from ATCC, Manassas, VA, USA), were cultured in high-glucose Dulbecco's modified Eagle's medium (DMEM) (Thermo Fisher Scientific, USA) containing 10% (v/v) FBS and penicillin/streptomycin. THP-1 cells, a human leukemia monocyte cell line (purchased from ATCC, Manassas, VA, USA), were cultured in complete RPMI medium with 10% (v/v) FBS and penicillin/streptomycin. All cells were cultured in a humidified incubator with 5% CO_2 at 37 °C.

2.4. Isolation and purification of EVs

EVs were purified by ultracentrifugation, as described in our previous study [22]. Spleen primary T lymphocytes were cultured in medium with EV-free serum (which was depleted of endogenous EVs by ultracentrifugation at 120000 g overnight at 4 °C prior to use) and were treated with or without 100 μmol/L homocysteine (H4628, Sigma-Aldrich, St. Louis, MO, USA). T-lymphocyte culture supernatants or human plasma were consecutively centrifuged at 300 g for 10 min at 4 °C, 2000 g for 10 min at 4 °C, and 10000 g for 45 min at 4 °C to remove cells and cell debris. The resulting supernatants were filtered through a 0.2 μm filter (PN4612; Pall, Westborough, MA, USA) to remove particles larger than 200 nm. The filtered supernatants were ultracentrifuged (Beckman Coulter, Brea, CA, USA) at 120000 g for 70 min at 4 °C to pellet the EVs. The condensed pellet was washed with ice-cold PBS and centrifuged again at 120000 g for another 70 min at 4 °C. The EV-enriched pellet was resuspended repeatedly in a small volume of PBS (approximately 150 μL). The concentrations of EV proteins were measured using the BCA Protein Assay Kit (Thermo Scientific, Waltham, MA).

2.5. Administration of macrophages with EVs

For determination of the effects of EVs on macrophages, EVs (10 μg/mL) isolated from T lymphocyte culture supernatants were cocultured with primary macrophages or RAW264.7 cells. EVs (20 μg/mL) isolated from human plasma were cocultured with THP-1 cells. After 24 h, the levels of various genes in RAW264.7 cells were evaluated by qPCR, and RAW264.7, primary macrophage or THP-1 cell lipid peroxidation and iron accumulation were detected. After 48 h, the expression of different proteins in RAW264.7 cells was measured by Western blots, and macrophage migration was measured by a Transwell experimental system. For inhibition of EV internalization, macrophages or RAW264.7 cells were pretreated with 20 μmol/L Dynasore (HY-15304, MedChemExpress, USA) for 1 h. For inhibition of lipid peroxidation, cells were pretreated with ferropstatin-1 (Fer-1, 5 μmol/L) (HY-100579, MedChemExpress, USA) or liproxstatin-1 (Lip-1, 1 μmol/L) (SML1414, Sigma-Aldrich, St. Louis, MO, USA) for 1 h. For prevention of free iron from engaging in chemical reactions, RAW264.7 cells were pretreated with the iron chelating agent deferoxamine mesylate (DFOM) (10 μmol/L) (HY–B0988, MedChemExpress, USA), while THP-1 cells were pretreated with DFOM (20 μmol/L) for 2 h.

2.6. Morphometric, histological and immunofluorescence analysis

Mice were euthanized and perfused through the left ventricle with

PBS. The aortas were isolated carefully, fixed with 4% paraformaldehyde for 4–6 h and then fixed on black cloth for photography. The diameters of the aortas were measured using ImageJ software (National Institutes of Health, Bethesda, ML, USA). Infrarenal abdominal aortas were embedded in OCT compound and cut into serial frozen sections (7 μm thick, 70 μm apart). A Verhoef-Van Gieson Staining Kit (Baso Diagnostics, Inc., China) was used to analyze elastin degradation in the infrarenal abdominal aortas. Elastin degradation was graded on a scale of 1–4, where 1 indicates <25% degradation, 2 indicates 25–50% degradation, 3 indicates 50–75% degradation, and 4 indicates >75% degradation.

For immunofluorescence staining, mouse aortic sections were stained with primary antibodies against CD3ε (99940, Cell Signaling Technology, Danvers, MA), F4/80 (ab6640, Abcam, Cambridge, MA, USA), MMP2 (ab92536, Abcam, Cambridge, MA, USA), MMP9 (ab38898, Abcam, Cambridge, MA, USA), Gpx4 (ab219592, Abcam, Cambridge, MA, USA) and Slc7a11 (ab216876, Abcam, Cambridge, MA, USA) overnight at 4 °C, followed by fluorescent secondary antibodies (Alexa Fluor 647/555/488 goat anti-rabbit/mouse/rat IgG) for 1 h at 37 °C. All immunofluorescence analyses were performed at room temperature using a Leica Microsystems instrument (Fluorescence Light DM4000B and Confocal TCS SP8 Microscopes). To quantify the mean fluorescence intensity (MFI) of MMP9 and MMP2, fluorescent images were converted to grayscale firstly, and the image brightness intensity was measured using ImageJ. The MFI of MMPs in the LckCrePKM2$^{fl/fl}$ group was normalized to it in the PKM2$^{fl/fl}$ group.

For immunohistochemistry staining, frozen sections were washed with PBS twice, and then, 3% H_2O_2 for 10 min was applied to block endogenous peroxidase. The sections were blocked with goat serum at 37 °C for 30 min and then incubated with mouse monoclonal anti-4-hydroxynonenal antibody (anti-4-HNE antibody, MAB3249, R&D Systems, USA) at a 1:50 dilution for 1 h at room temperature. The antigen–antibody reactions were detected with secondary polyperoxidase-anti-mouse/rabbit IgG (E-IR-R217, Elabscience, Wuhan, China) and visualized with DAB for 5 min. The sections were lightly counterstained, dehydrated with an ethanol series, cleared in xylene and coverslipped before examination by light microscopy.

2.7. Western blot

Protein concentrations were measured using the BCA Protein Assay Kit and then used for SDS-PAGE and transferred onto nitrocellulose membranes by wet electrophoretic transfer. The membranes were blocked and incubated with primary antibodies against Slc7a11, Gpx4, Slc40a1 (A14884, ABclonal, Wuhan, China), TFR (ab214039, Abcam, Cambridge, MA, USA), β-actin (ABclonal, Wuhan, China), and GAPDH (ABclonal, Wuhan, China) overnight at 4 °C and with appropriate HRP-conjugated secondary antibodies (Abclonal, Wuhan, China) for 1 h at room temperature. An Odyssey infrared imaging system (Li-Cor Biosciences, Lincoln, NE, USA) was used for visualization after coating with Immobilon Western Chemiluminescent HRP Substrate (Millipore Corporation, MA, USA).

2.8. Quantitative PCR measurement of mRNA levels

Total RNA was extracted using TRIzol reagent (15596018; Thermo Fisher Scientific), and mRNA was isolated using the reverse transcription (RT) system 5X All-In-One RT MasterMix Kit (G490; Applied Biological Materials, Richmond, BC, Canada). Quantitative RT-PCR was then used to measure the cDNA content with an Mx3000 Multiplex Quantitative PCR (qPCR) System (Stratagene California, San Diego, CA, USA) and SYBR Green I fluorescence. The results were normalized to the *GAPDH* mRNA levels and analyzed using Stratagene Mx3000 software. The primer sequences used were listed as follows: glutathione peroxidase 4 (*Gpx4*) (forward 5′-TGTGCATCCCGCGATGATT-3′; reverse 5′-CCCTGTACTTATCCAGGCAGA-3′), solute carrier family 7 member 11 (*Slc7a11*) (forward 5′-AGGGCATACTCCAGAACACG-3′; reverse 5′-GGACCAAAGACCTCCAGAATG-3′), solute carrier family 40 member 1 (*Slc40a1*) (forward 5′-GCGATCACAATCCAAAGGGAC-3′; reverse 5′-TTGGTTAGCTGGTCAATCCTTC-3′), transferrin receptor (*Tfrc*) (forward 5′-GTTTCTGCCAGCCCCTTATTAT-3′; reverse 5′-GCAAGGAAAGGATATGCAGCA-3′), prostaglandin-endoperoxide synthase 2 (*Ptgs2*) (forward 5′-TTCCAATCCATGTCAAAACCGT-3′; reverse 5′-AGTCCGGGTACAGTCACACTT-3′), catalase (*Cat*) (forward 5′-GGAGGCGGGAACCCAATAG-3′; reverse 5′-GTGTGCCATCTCGTCAGTGAA-3′), superoxide dismutase 1 (*SOD1*) (forward 5′- ATGGCGATGAAAGCGGTGT-3′; reverse 5′-CCTTGTGTATTGTCCCCATACTG-3′), and *GAPDH* (forward 5′- AGGTCGGTGTGAACGGATTTG-3′; reverse 5′-GGGGTCGTTGATGGCAACA-3′).

2.9. PBMC isolation

Human blood samples were collected in EDTA-treated tubes immediately before surgery. PBMCs were isolated from 5 mL of blood by centrifugation on a Ficoll-Paque density gradient (17144002, Cytiva, USA). Whole blood was centrifuged at 1800 rpm for 5 min at 25 °C, the upper layer plasma was used to isolate EVs, and the cells were transferred into a 50 mL conical tube prefilled with 10 mL of PBS for dilution. This diluted blood was aspirated and carefully decanted into another Ficoll-Paque-containing 50 mL conical tube to centrifuge at 2500 rpm for 25 min at 25 °C with no braking. Centrifugation resulted in an upper layer of plasma with a cloudy band of PBMCs and a lower layer of erythrocytes and polymorphonuclear cells separated by Ficoll-Paque PLUS. After centrifugation, the cloudy PBMC band was collected using a sterile transfer pipette and added to a 15 mL conical tube prefilled with 10 mL of PBS. The capped 15 mL conical tube was further mixed by inversion and centrifuged at 1800 rpm for 10 min at 4 °C. The supernatant was carefully aspirated, and the cell pellet was resuspended in 10 mL of fresh PBS and centrifuged for a subsequent 10 min at 1800 rpm at 4 °C. Following this centrifugation step, the supernatant was again carefully aspirated without disturbing the cell pellet, and PBMCs were resuspended in PBS.

2.10. Aortic single cell preparation

Preparation of the single-cell suspension of the aortic cells was performed by following a previously described enzymatic digestion protocol [29]. In brief, the aortic tissues were cut and digested with an enzyme solution (450 U/mL collagenase type I, 125 U/mL collagenase type XI, 60 U/mL hyaluronidase type I-s, and 60 U/mL DNase I) for 1.5 h at 37 °C. All these enzymes were purchased from Sigma-Aldrich (St. Louis, MO, USA). The cell suspension was strained through a 70 μm filter and washed three times with PBS. The cells were resuspended in RPMI 1640 and subjected to flow cytometric analysis.

2.11. Flow cytometric analysis

For analysis of intracellular PKM2, cells infiltrated in vascular lesions of mice were stained with anti-CD4 antibody (550057, BD Biosciences, Franklin Lakes, NJ, USA) and anti-PKM2 antibody (4053s, Cell Signaling Technology, Danvers, MA) overnight at 4 °C, followed by fluorescent secondary antibody (Alexa Fluor 488 goat anti-rabbit IgG) for 1 h at room temperature. PBMCs isolated from human whole blood were stained with FITC mouse anti-human CD3 monoclonal antibody [UCHT1] (ab34275, Abcam, Cambridge, MA, USA) and PE conjugated anti-PKM2 antibody (89367s, Cell Signaling Technology, Danvers, MA) overnight at 4 °C. For analysis of intracellular ROS and the amount of lipid peroxides, RAW264.7 cells were stained with DCFH-DA (S0033S, Beyotime, Shanghai, China) or BODIPY 581/591 C11 (D-3861, BD Biosciences, Franklin Lakes, NJ, USA) probe according to the manufacturer's protocol. Lipid oxidation was determined by monitoring the green fluorescence increase of the oxidation product of BODIPY. For

detection of the ratios of apoptotic and necrotic cells, all suspended RAW264.7 cells in the supernatant and digested adherent cells were collected. After centrifugation, the cells were washed twice with binding buffer, resuspended in 300 μL of the same buffer and incubated at room temperature for 15 min with 5 μL of Annexin V-FITC (CTK007–100, M&C Gene, Beijing, China). Then, 5 μL of PI was added for another 5 min. Before flow cytometric analysis, 200 μL binding buffer was added to each sample. The cells were analyzed using a FACSCalibur flow cytometer (BD Biosciences, Franklin Lakes, NJ, USA) and FlowJo software (Treestar, Ashland, OR, USA).

2.12. Migration assays

EVs were cocultured with immortalized RAW264.7 cells. After 24 h, the RAW264.7 cells were washed once with PBS, which was replaced with 5 mM HEPES medium (without FBS) for subsequent assays. Migration of cells was observed by a TAXIScan-FL cell dynamic visualization system (Effector Cell Institute, Japan). The cells were aligned at the start line on the edge of the channel, and 2 ng/mL MCP-1 (250-10-10, PeproTech, USA) was added as a chemokine on the other edge of the channel. Subsequently, time-lapse imaging was recorded (taking an image every 3 s for a total of 3 h). Acquired time-lapse images were analyzed in the TAXIScan-FL cell dynamic visualization and individual cell-tracking analysis systems. During analysis, one cell was selected at the first time point and clicked at the location of it, and then followed the cell through all time-points. Repeated it for 15–20 representative cells of each group. Finally, a new window with a series results (track, slice, real-time velocity, distance and direction) appeared and the dataset could be saved. The cell trajectory plots of 5 representative cells in each group were analyzed by the Chemotaxis plugin (http://ibidi.com/fileadmin/products/software/chemotaxis_tool/chemotaxis_tool.jar) of ImageJ/Fiji (http://fiji.sc/) as described in the Instructions of the Chemotaxis and Migration Tool Version 1.01.

Transwell migration assays were performed by adding peritoneal macrophages or THP-1 cells to the upper chamber and adding MCP-1 (20 ng/mL) to the lower chamber (24-well plate with 8.0 μm Transparent PET Membrane, Falcon, BD Biosciences, San Jose, CA, USA). Peritoneal macrophages or THP-1 cells were incubated with EVs or EVs plus the lipid peroxidation inhibitor Fer-1 or Lip-1 or the iron chelating agent DFOM. A crystal violet staining kit (C0121, Beyotime, Shanghai, China) was used to stain the migrated peritoneal macrophages after 48 h of incubation. Cells were counted from 5 random microscope fields for each sample in 5 independent experiments. THP-1 cells were collected after 48 h, and the number of cells in the upper and lower chambers was counted by flow cytometry. The migration ratio was calculated.

2.13. Lipid peroxidation and iron analysis

The intracellular concentrations of lipid peroxidation (LPO), malondialdehyde (MDA), antioxidant glutathione (GSH), NADPH/$NADP^+$ ratio and iron concentrations were measured with standard protocols by assay kits (Nanjing Jiancheng Bioengineering Institute, Nanjing, China).

Fe^{2+} in peritoneal macrophages or THP-1 cells was measured by a Phen Green SK probe (GC40243-500, Glpbio, USA). Cells suspended in HBSS were loaded with 20 μmol/L Phen Green SK, a fluorescent iron chelator, for 15 min at 37 °C. After dye loading, the cells were washed three times with HBSS. The fluorescence of Phen Green SK, which represented the release of free iron, was monitored at an excitation wavelength of 488 nm and an emission wavelength of 530 nm. The intracellular free iron level was inversely proportional to the Phen Green fluorescence intensity.

2.14. Metabolomics analysis

EVs were purified by ultracentrifugation from T-lymphocyte culture supernatants. Then, EV metabolomics was performed by HPLC-MS/MS analysis as reported in our previously published study [22]. Metabolite abundance was normalized using EV concentrations. Metabolite concentrations were determined with MetaboAnalyst software.

2.15. Statistical analysis

All statistical analyses were performed using Prism v.7.0 (GraphPad Software, La Jolla, CA, USA), and all data from ≥3 independent experiments are shown as the mean ± SEM. Statistical analysis was performed with unpaired Student's *t*-test or Fisher's exact test for comparisons between two groups and with one-way ANOVA followed by Tukey's test for multiple comparisons. A value of $P < 0.05$ was considered statistically significant.

3. Results

3.1. T lymphocyte-specific PKM2 deficiency attenuates elastase-induced AAA and decreases macrophage numbers in the vascular adventitia of mice

The acceleration of glucose metabolism is associated with AAA development [30]. Enhanced glycolytic activity in the aortic wall contributes to the pathogenesis of aneurysm development, although the mechanisms are unclear. In the present study, we first used WT mice to develop an elastase-induced AAA model. Two weeks after elastase induction, we observed a significant expansion of the infrarenal abdominal aorta (1.414 ± 0.030 mm in the saline-treated sham group and 2.202 ± 0.154 mm in the elastase-treated AAA group; Fig. 1A). More importantly, aortas were digested into single-cell suspensions for FACS analysis, and we found that the expression of PKM2, the last rate-limiting enzyme in glycolysis, was significantly increased in these infiltrated T lymphocytes (Fig. 1B). To further examine the role of T lymphocyte PKM2 in elastase-induced AAA, we used T lymphocyte-specific PKM2 knockout mice (LckCrePKM2$^{fl/fl}$ mice) and PKM2$^{fl/fl}$ mice. Two weeks after elastase induction, we observed a significant expansion of the infrarenal abdominal aorta in the PKM2$^{fl/fl}$ mice, and T lymphocyte-specific PKM2 knockdown markedly reduced the expansion of the infrarenal abdominal aorta (2.095 ± 0.126 mm in the PKM2$^{fl/fl}$ group and 1.222 ± 0.093 mm in the LckCrePKM2$^{fl/fl}$ group; Fig. 1C). Notably, in the PKM2$^{fl/fl}$ mice, the incidence of AAA was 88.89% (8/9), while the incidence of AAA was decreased dramatically in the LckCrePKM2$^{fl/fl}$ mice (22.22%, 2/9; Fig. 1D). Moreover, Verhoef-Van Gieson staining showed that T lymphocyte-specific PKM2 knockdown significantly inhibited elastin degradation in AAA (Fig. 1E). Upregulation of MMP9 and MMP2 levels is a well-recognized cause of AAA. In the present study, MMP2 and MMP9 levels were both downregulated in vascular lesions of the LckCrePKM2$^{fl/fl}$ mice compared with those in the PKM2$^{fl/fl}$ mice (Fig. 1F). These results indicate that T lymphocyte PKM2 plays a key role in the development of elastase-induced AAA.

Then, we further investigated the potential mechanisms by which T lymphocyte PKM2 mediated AAA formation. AAA is mainly characterized by extensive vascular inflammation. We stained AAA tissues for a macrophage marker (F4/80) and found that compared to those of the PKM2$^{fl/fl}$ mice, macrophages that infiltrated into the vascular adventitia of AAA lesions were dramatically reduced in the LckCrePKM2$^{fl/fl}$ mice (Fig. 1G). We next collected elastase-treated infrarenal abdominal aortas from the PKM2$^{fl/fl}$ and LckCrePKM2$^{fl/fl}$ groups and then digested them into single-cell suspensions for the following flow cytometric assay. Data confirmed that T-lymphocyte PKM2 knockout significantly inhibited the accumulation of F4/80$^+$ macrophages in the infrarenal abdominal aortic wall during AAA formation (Fig. 1H). This finding indicates that there is crosstalk between T lymphocytes and macrophages, which may be involved in elastase-induced AAA development.

In response to chemokines, cytokines and products of extracellular matrix degradation, macrophages are recruited and accumulate in AAA

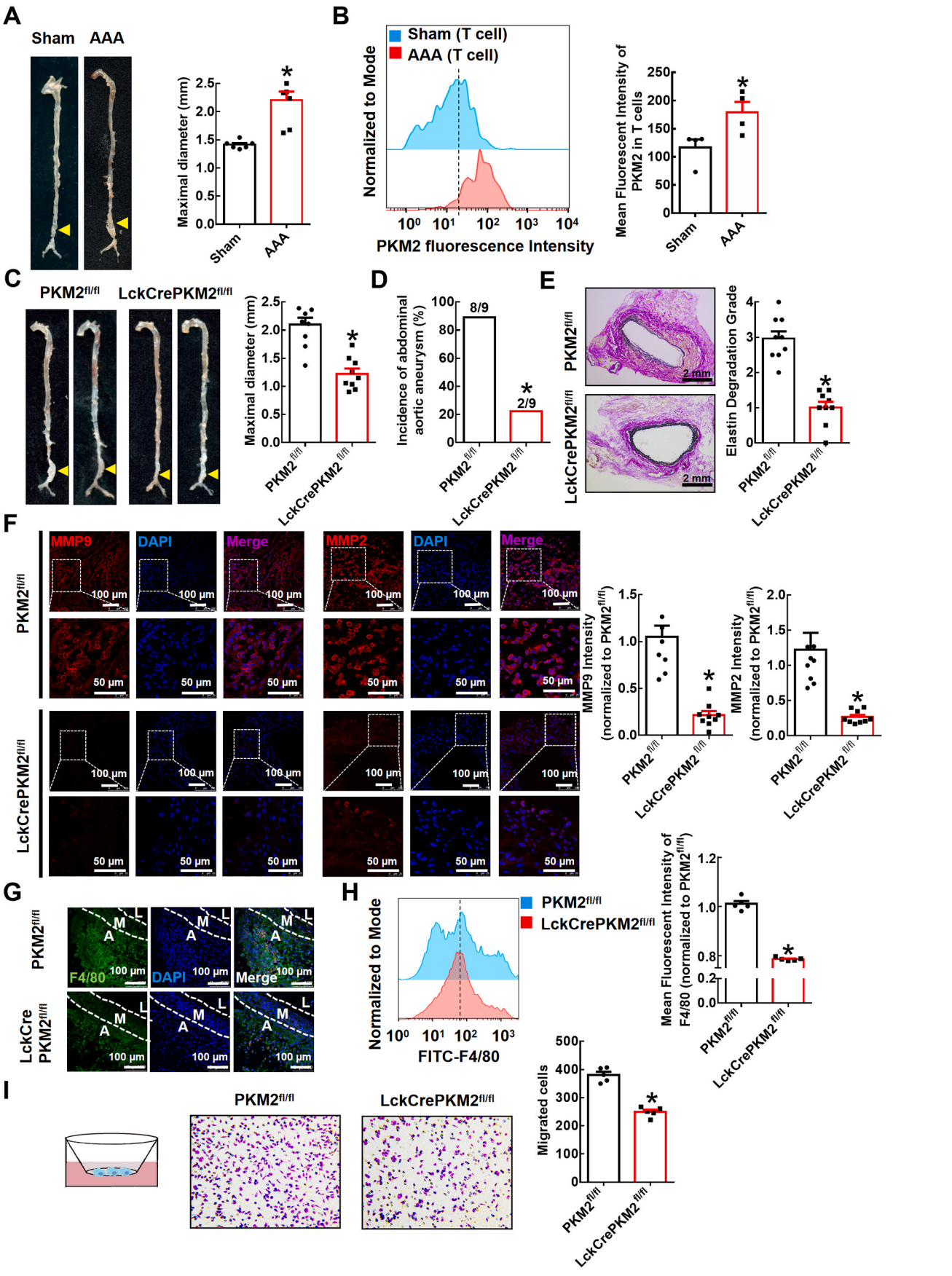

(caption on next page)

Fig. 1. T lymphocyte-specific PKM2 deficiency attenuates elastase-induced abdominal aortic aneurysm (AAA) and decreases macrophage numbers in the vascular adventitia of mice.
Infrarenal abdominal aortas of 10-week-old wild-type (WT) mice were treated with elastase for 2 weeks to induce AAA (A-B; n = 4–6). (A) Representative photographs of the infrarenal abdominal aortas and quantification of maximal diameters of the infrarenal abdominal aortas is shown in the right panel. (B) Cells infiltrating vascular lesions were stained with fluorescently conjugated anti-CD4 and PKM2 pAbs and then analyzed by flow cytometry. Quantification of T lymphocyte PKM2 expression in the infrarenal abdominal aortas is shown in the right panel. The infrarenal abdominal aortas of 10-week-old $PKM2^{fl/fl}$ and $LckCrePKM2^{fl/fl}$ mice were treated with elastase for 2 weeks to induce AAA (C–I; n = 5–9). (C) Representative photographs of the infrarenal abdominal aortas and quantification of maximal diameters of infrarenal abdominal aortas are shown. (D) Incidences of AAA in the elastase-treated $PKM2^{fl/fl}$ and $LckCrePKM2^{fl/fl}$ mice. (E) Representative Verhoef–Van Gieson staining and statistical analysis of elastin degradation in the infrarenal abdominal aortas of the $PKM2^{fl/fl}$ and $LckCrePKM2^{fl/fl}$ mice. (F) Representative immunofluorescence staining of MMP9 and MMP2 in aortic tissues. Every microscopy figure is presented as a total view of the field above and a cutout of that field with a high magnification below. DAPI indicated the cell nucleus. The right panels show the quantification of MMP9 and MMP2 fluorescent expression. Scale bar, 50 μm and 100 μm. (G) Representative immunofluorescence staining of macrophages (anti-F4/80, green) in the infrarenal abdominal aortas. Scale bar, 100 μm. A: tunica adventitia; M: tunica medium; L: tunica lumen. (H) Expression of F4/80 tested by flow cytometry in the elastase-induced vascular lesions of the infrarenal abdominal aortas. Quantitation is shown in the right panel. (I) Left panel: Schematic illustration of the Transwell experimental system. Macrophages were added to the upper chamber, with MCP-1 (20 ng/mL) in the lower chamber; after 48 h of incubation at 37 °C, cells that migrated to the bottom chamber were quantified. Representative images of crystal violet staining were captured to indicate migrated peritoneal macrophages and are shown in the middle panel. The quantitative number of migrated cells is shown in the right panel. Cells were counted from 5 random microscope fields for each sample in 5 independent experiments. The data are presented as the mean ± SEM. (A–B) $*p < 0.05$, compared with the sham group. (C–F, H–I) $*p < 0.05$, compared with the $PKM2^{fl/fl}$ group. The data were analyzed using Student's *t*-test or Fisher's exact test (D). (For interpretation of the references to colour in this figure legend, the reader is referred to the Web version of this article.)

lesions and then participate in vascular remodeling. Macrophages in vascular lesions were specifically decreased in the $LckCrePKM2^{fl/fl}$ mice, which may be one of the major causes of the decreased AAA incidence in these mice. We subsequently performed a Transwell migration assay using isolated peritoneal macrophages of the $PKM2^{fl/fl}$ and $LckCrePKM2^{fl/fl}$ AAA mice *ex vivo* (Fig. 1I). Decreased migration of macrophages in the $LckCrePKM2^{fl/fl}$ AAA mice was observed compared to that in the $PKM2^{fl/fl}$ AAA mice when MCP-1 was added to the lower chamber (Fig. 1I). This finding suggests that T lymphocytes may increase macrophage migration into the vascular adventitia through PKM2, which may subsequently promote AAA.

3.2. EVs derived from PKM2-activated T lymphocytes promote macrophage migration in vitro

EVs mediate intercellular communication and are involved in various diseases [31]. We have reported that EVs derived from PKM2-activated T lymphocytes are one of the main ways to aggravate atherosclerosis [22]. It is worth discussing whether T lymphocyte-derived EVs mediate the progression of AAA by affecting macrophage migration via PKM2. In addition, our previous study has demonstrated that Hcy increases PKM2 protein expression and activity and could be used as a potential PKM2 activator [26]. To explore the effects of T lymphocyte-derived EVs mediated by PKM2 on macrophage migration *in vitro*, we isolated splenic T lymphocytes from the $PKM2^{fl/fl}$ or $LckCrePKM2^{fl/fl}$ mice, treated them with or without Hcy stimulation, and subsequently purified EVs from T lymphocyte culture supernatants. These EVs were cultured with RAW264.7 cells for 24 h, and then, the treated RAW264.7 cells were plated into the individual cell-tracking system (Fig. 2A). After an additional 3 h, the migration of RAW264.7 cells was observed by a cell dynamic visualization system. Time-lapse records followed by single-cell tracking were used to evaluate cell migration. We found that the cells became flatter and more spread during the period (Supplementary Movies 1-4).

We in turn assessed the individual cell trajectories of RAW264.7 cells after 24 h of treatment with EVs (10 μM) derived from different T lymphocytes with or without PKM2. With live cell imaging analysis, representative phase contrast images of EV-treated cells for 3 h were recorded, indicating that cells in each group migrated to the side of MCP-1 (Fig. 2A). Compared with the $PKM2^{fl/fl}$-C-EVs, EVs derived from PKM2-null T lymphocytes ($LckCrePKM2^{fl/fl}$-C) strongly attenuated cell migration; EVs from PKM2-activated T lymphocyte ($PKM2^{fl/fl}$-Hcy)-treated RAW264.7 cells migrated farther, and the number of migrated cells increased, which was partly inhibited by the $LckCrePKM2^{fl/fl}$-Hcy-EVs (Fig. 2B). By an automatic tracking system, we showed the final position of 15–20 representative cells in each group and their traces from an origin and determined the real-time velocity and multiple cell directions within 3 h (Fig. 2C). In Fig. 2D, the representative cell migration trajectories of different experimental groups were plotted with a common origin for RAW264.7 cells. Consequently, we quantified the average accumulated distance (μm) within 3 h for approximately 15–20 cells in each experimental group. The $PKM2^{fl/fl}$-C-EV-treated cells presented a mean of 76.79 ± 7.83 μm in accumulated distances, and the $PKM2^{fl/fl}$-Hcy-EV-treated cells showed a significant increase (115.80 ± 16.99 μm), whereas the $LckCrePKM2^{fl/fl}$-C-EV-treated cells showed a marked reduction (52.26 ± 4.80 μm). Compared with the $PKM2^{fl/fl}$-Hcy-EV-treated cells, the $LckCrePKM2^{fl/fl}$-Hcy-EV-treated cells totally reversed the increased accumulated distances by Hcy to 74.48 ± 7.47 μm (Fig. 2E). Therefore, EVs derived from T lymphocytes regulate macrophage locomotion via PKM2.

3.3. EVs derived from PKM2-activated T lymphocytes promote lipid peroxidation in macrophages in vitro

AAA pathogenesis is associated with inflammation, in which the production of ROS and oxidative stress are involved [32]. Studies have shown that lipid peroxidation of tumor cells affects their migration [14]. To define the underlying mechanisms by which PKM2-mediated T lymphocyte-derived EVs regulate macrophage migration, we treated RAW264.7 cells or peritoneal macrophages with different EVs and then examined intracellular lipid peroxidation. The data showed that the levels of lipid peroxidation products (e.g., lipid peroxidation [LPO] and malondialdehyde [MDA]) were both increased in the RAW264.7 cells treated with EVs from the $PKM2^{fl/fl}$-Hcy group compared to EVs from the $PKM2^{fl/fl}$-C group. Macrophages in the $LckCrePKM2^{fl/fl}$-C-EV-treated group showed a significant decrease in lipid peroxidation compared with the $PKM2^{fl/fl}$-C group. And the lipid peroxidation product elevation was decreased significantly in the $LckCrePKM2^{fl/fl}$-Hcy-EV-treated cells compared with macrophages in the $PKM2^{fl/fl}$-Hcy-EV-treated group (Fig. 3A and B). Consistently, $PKM2^{fl/fl}$-Hcy-EVs significantly increased and $LckCrePKM2^{fl/fl}$-C-EVs obviously decreased the macrophage intracellular ROS level and the amount of lipid peroxides in cellular membranes, as indicated by the DCFH-DA and BODIPY-C11 probe staining with flow cytometry, compared with the $PKM2^{fl/fl}$-C-EVs (Fig. 3C and D). $LckCrePKM2^{fl/fl}$-Hcy-EVs inhibited the elevated intracellular concentration of ROS and lipid peroxides in macrophages stimulated by the $PKM2^{fl/fl}$-Hcy-EVs (Fig. 3C and D). Additionally, the changes in GSH levels and the NADPH/$NADP^+$ ratio, indicating antioxidant capacity, were opposite to the changes in lipid peroxidation products (Fig. 3E and F).

The amino acid antiporter system Xc-mediates the exchange of extracellular cystine and intracellular glutamate across the plasma

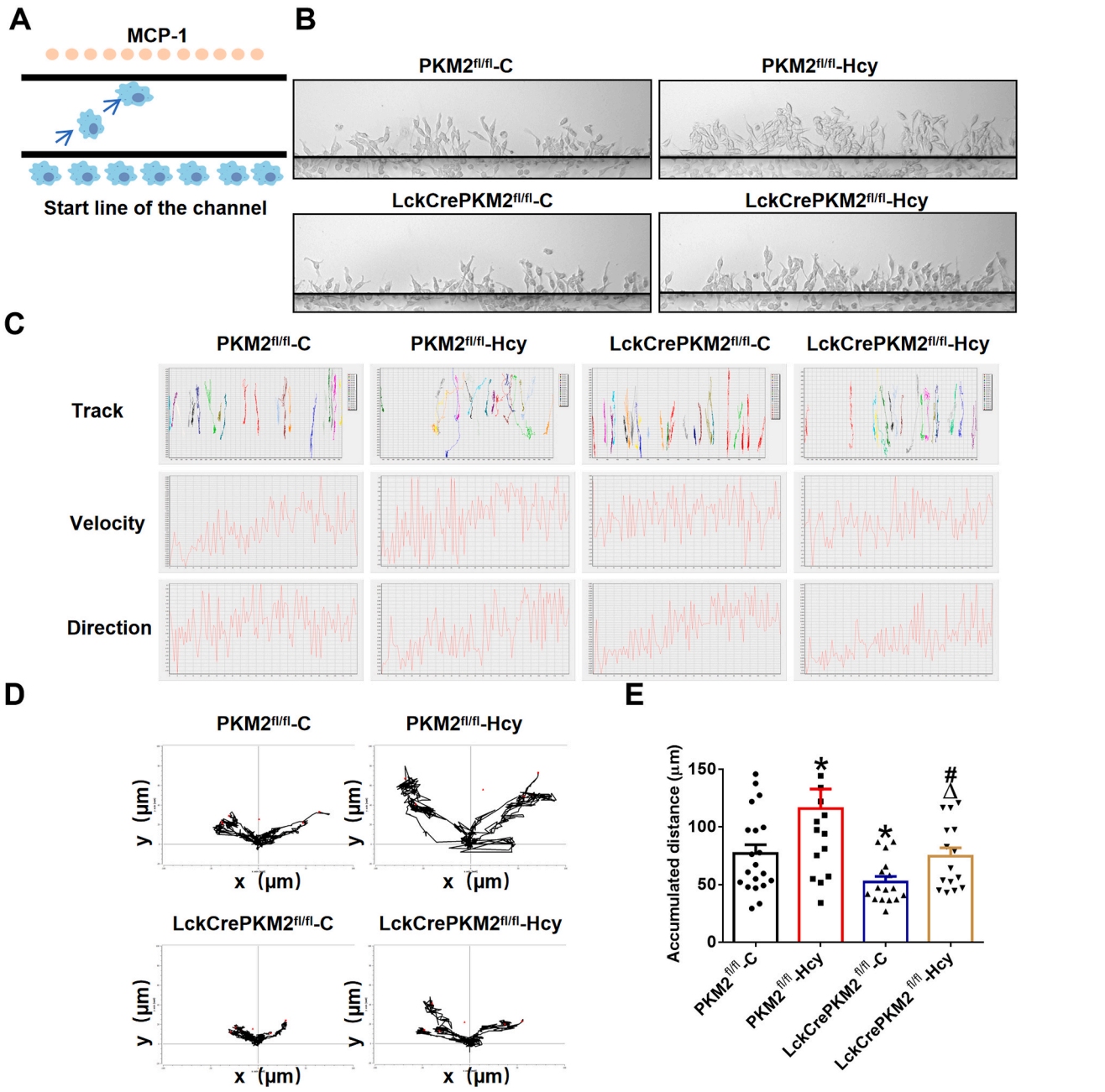

Fig. 2. Extracellular vesicles derived from PKM2-activated T lymphocytes promote macrophage migration *in vitro*.
T lymphocytes from the PKM2$^{fl/fl}$ or LckCrePKM2$^{fl/fl}$ mice were isolated and then treated with or without Hcy (100 mmol/L) *in vitro*. After 48 h, EVs were isolated from cell culture supernatants. Equal concentrations (10 μg/mL) of EVs from the PKM2$^{fl/fl}$-C, PKM2$^{fl/fl}$-Hcy, LckCrePKM2$^{fl/fl}$-C or LckCrePKM2$^{fl/fl}$-Hcy T lymphocytes cultured with RAW264.7 cells for an additional 24 h. Migration of RAW264.7 cells by MCP-1 was observed by the cell dynamic visualization system TAXIScan-FL. (A) Schematic illustration of the TAXIScan-FL experimental system. RAW264.7 cells were washed with PBS, which was replaced with medium containing 5 mM HEPES without FBS for the assay. The cells at the start line on the edge of the channel were aligned, MCP-1 (2 ng/mL) was added as a chemokine on the other edge of the channel, and time-lapse image recording was performed (taking an image every 30 s for 3 h). (B) Representative images of RAW264.7 cells were captured at 3 h after migration. (C) Automatic tracking of every cell in the channel showed the final position of 15–20 representative cells of each group and its movement traces from the origin position. Determination of the real-time velocity and the direction of multiple migrated cells within 3 h is shown in the lower panel. (D) Trajectory plots showing 5 representative RAW264.7 cells in each group over 3 h. (E) Quantitative analysis of the average accumulated distance (μm) of RAW264.7 cells within 3 h. The data are presented as the mean ± SEM. *$p < 0.05$, compared with PKM2$^{fl/fl}$-C. #$p < 0.05$, compared with LckCrePKM2$^{fl/fl}$-C. Δ$p<0.05$, compared with PKM2$^{fl/fl}$-Hcy. The data were compared using one-way ANOVA followed by Tukey's multiple comparison test. n = 15–20.

membrane and is important for the synthesis of GSH, which prevents lipid peroxidation and protects cells against lipid peroxidation [33]. Actually, the activity of system Xc-usually positively correlates with the expression level of its light chain encoded by Slc7a11 [34]. The accumulation of lipid peroxidation products is normally dissipated by the antioxidant enzyme Gpx4. The Slc7a11-Gpx4 axis has a protective effect on lipid peroxidation. In the present system, the protein levels of Gpx4 in macrophages were markedly decreased by the PKM2$^{fl/fl}$-Hcy-EVs, accompanied by decreased *Gpx4* and *Slc7a11* gene expression, while the protein levels of Gpx4, Slc7a11 and *Gpx4* were significantly increased by the LckCrePKM2$^{fl/fl}$-C-EVs (Fig. 3G and H). Additionally, the expression of another peroxidase (e.g., prostaglandin endoperoxidase synthase 2,

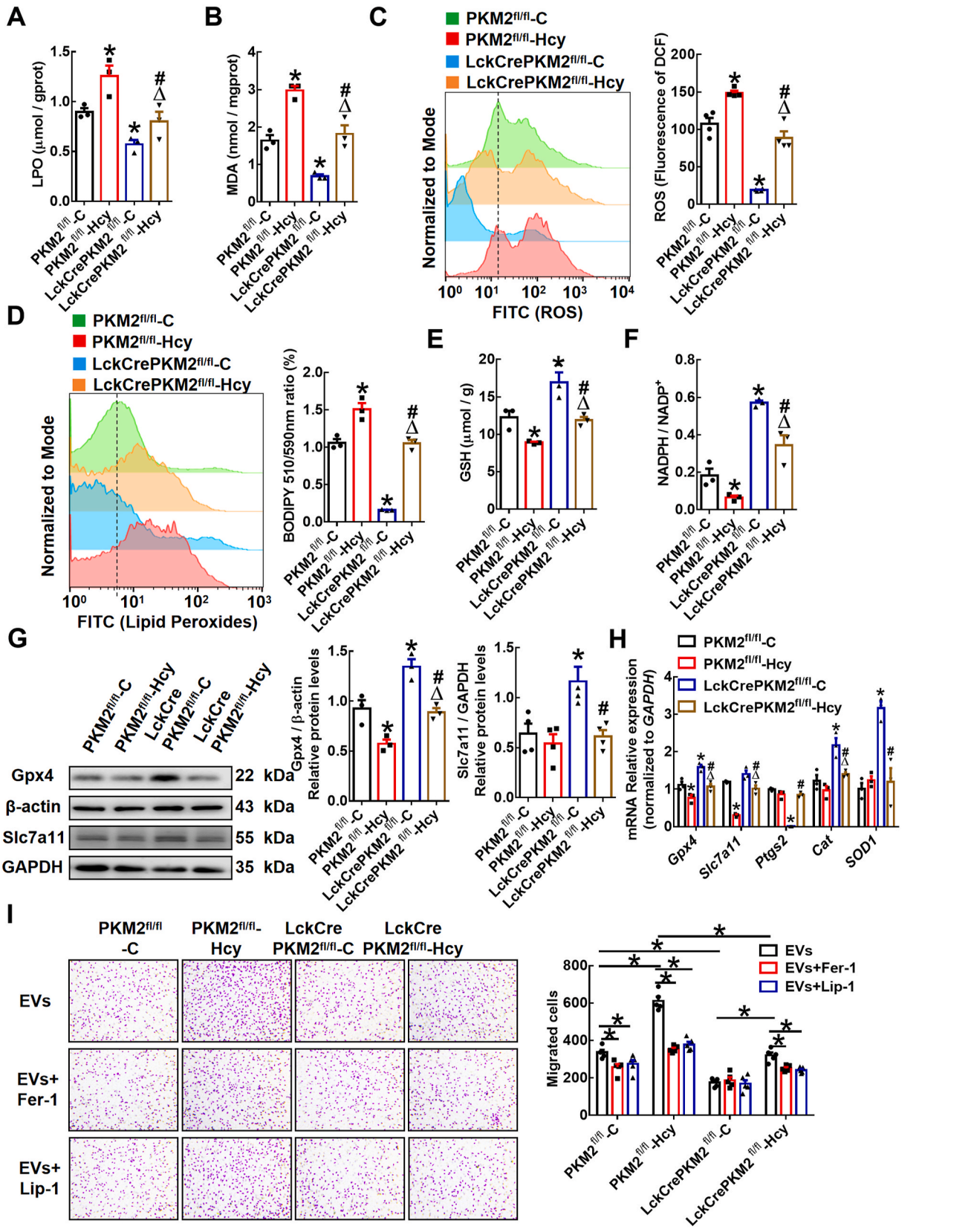

(caption on next page)

Fig. 3. Extracellular vesicles derived from PKM2-activated T lymphocytes promote lipid peroxidation in macrophages.
Equal concentrations (10 μg/mL) of EVs from the $PKM2^{fl/fl}$-C, $PKM2^{fl/fl}$-Hcy, $LckCrePKM2^{fl/fl}$-C or $LckCrePKM2^{fl/fl}$-Hcy T lymphocytes were cultured with RAW264.7 cells for 24 h n = 3–5. Quantification of intracellular lipid peroxidation (LPO) (A) and malondialdehyde (MDA) (B). (C) Intracellular ROS levels in RAW264.7 cells were measured by a DCFH-DA probe through flow cytometric analysis and quantification. (D) Flow cytometric analysis of BODIPY 581/591 C11 and quantification of the oxidized BODIPY-C11 (emission: 590 nm)/reduced BODIPY-C11 (emission: 510 nm) ratio in RAW264.7 cells. Measurement of the antioxidant GSH (E) and NADPH/$NADP^+$ ratio (F) in the RAW264.7 cells treated with different EVs. (G) Protein expression of Gpx4 and Slc7a11 was measured via Western blots, and the Gpx4 and Slc7a11 protein levels (relative to β-actin or GAPDH) in RAW264.7 cells was quantified after EV treatment for 48 h. (H) Gene expression levels of *Gpx4*, *Slc7a11*, *Ptgs2*, *SOD1* and *Cat* were measured via qPCR in RAW264.7 cells at 24 h after treatment with EVs. (I) Transwell migration assays of EV (10 μg/mL)-treated peritoneal macrophages in the upper chamber that migrated toward MCP-1 (20 ng/mL) in lower chamber with or without the lipid peroxidation inhibitors ferropstatin-1 (Fer-1, 5 μmol/L) or liproxstatin-1 (Lip-1, 1 μmol/L). Representative images of crystal violet staining were captured at 48 h after incubation to indicate migrated cells, and quantification of the migrated cells is shown. Cells were counted from 5 random microscope fields for each sample in 5 independent experiments. The data are presented as the mean ± SEM. (A–H) $*p < 0.05$, compared with $PKM2^{fl/fl}$-C. $\#p < 0.05$, compared with $LckCrePKM2^{fl/fl}$-C. $\Delta p<0.05$, compared with $PKM2^{fl/fl}$-Hcy. The data were compared using one-way ANOVA followed by Tukey's multiple comparison test. (For interpretation of the references to colour in this figure legend, the reader is referred to the Web version of this article.)

Ptgs2) in macrophages was downregulated, and the enzymatic antioxidants such as *SOD-1* and *Cat* were upregulated at mRNA level in these cells by treatment with the $LckCrePKM2^{fl/fl}$-C-EVs (Fig. 3H). These results showed that PKM2-mediated T lymphocyte-derived EVs increased macrophage lipid peroxidation production by regulating the cellular redox balance.

To further confirm the effects of lipid peroxidation on macrophage migration, we used specific lipid peroxidation inhibitors, such as ferrostatin-1 (Fer-1) and liproxstatin-1 (Lip-1), in our experimental system. Macrophages pretreated with Fer-1 or Lip-1 significantly inhibited the migration-promoting effect of the $PKM2^{fl/fl}$-Hcy-EVs but had no effect on the cells incubated with the $LckCrePKM2^{fl/fl}$-C-EVs (Fig. 3I). Additionally, as a promoter of lipid peroxidation, erastin (0.625–5 μmol/L) promoted macrophage migration (Supplementary Fig. 1). Therefore, T lymphocyte-derived EVs facilitate lipid peroxidation by inducing redox imbalance in macrophages and then promote macrophage migration via PKM2.

3.4. Inhibited vascular lipid peroxidation and promoted macrophage antioxidant capacity in a T lymphocyte-specific PKM2 knockout mouse model with AAA

To explore whether protection against lipid peroxidation is the underlying potential mechanism by which T lymphocyte-specific PKM2 knockout attenuates elastase-induced AAA and inhibits macrophage migration, we stained sections of elastase-treated infrarenal abdominal aortas for 4-hydroxynonenal (4-HNE), an advanced lipid peroxidation end product. The data showed that T-lymphocyte PKM2 knockout significantly inhibited the accumulation of 4-HNE induced by the redox imbalance in AAA (Fig. 4A). qPCR analysis showed that in peritoneal macrophages of the $LckCrePKM2^{fl/fl}$ mice with AAA, the gene expression levels of *Gpx4* and *Slc7a11* increased and the gene expression levels of *Ptgs2* decreased, indicating an enhanced antioxidant capacity and decreased oxidation, compared with those in the $PKM2^{fl/fl}$ mice (Fig. 4B). Additionally, we performed immunofluorescence staining of F4/80, slc7a11, and Gpx4 in AAA vascular tissues. Compared to that of the $PKM2^{fl/fl}$ mice, colocalization of macrophages with Gpx4 or slc7a11 in the lesions of the $LckCrePKM2^{fl/fl}$ mice with AAA increased (Fig. 4C and D), indicating an enhanced macrophage antioxidant capacity in the $LckCrePKM2^{fl/fl}$ mice. Thus, T lymphocyte-specific PKM2 knockout promotes macrophage antioxidant capacity in the vascular adventitia and ameliorates vascular lipid peroxidation *in vivo*.

3.5. EVs derived from PKM2-activated T lymphocytes promote iron accumulation in macrophages

Iron is essential to maintain the activity of many proteins involved in critical biochemical processes [35]. Given that excess iron disrupts macrophage redox homeostasis and catalyzes the propagation of ROS, leading to oxidative stress [36], we further explored whether the effects of PKM2-mediated T lymphocyte EVs on macrophage lipid peroxidation are related to intracellular iron levels. The data showed that the $PKM2^{fl/fl}$-Hcy-EVs enhanced and $LckCrePKM2^{fl/fl}$-C-EVs reduced the intracellular total Fe in RAW264.7 cells compared with that of the $PKM2^{fl/fl}$-C-EV-treated group (Fig. 5A). The increased intracellular iron in the RAW264.7 cells treated with $PKM2^{fl/fl}$-Hcy-EVs was partly reversed by $LckCrePKM2^{fl/fl}$-Hcy-EV treatment (Fig. 5A). Consistently, data on the intracellular free iron levels in peritoneal macrophages measured by Phen Green SK probe also showed that EVs from PKM2-activated T lymphocytes promote macrophage iron accumulation (Fig. 5B). As Phen green fluorescence is quenched by iron, the inverse of fluorescence was plotted for these dyes to represent relative levels of cellular iron. Furthermore, qPCR and Western blot analysis showed that $LckCrePKM2^{fl/fl}$-C-EVs increased the gene and protein expression levels of Slc40a1, which is an iron transporter critical for cellular iron release, and decreased the gene expression level of *Tfrc*, which is critical for transferrin uptake, while $PKM2^{fl/fl}$-Hcy-EVs decreased Slc40a1 protein expression and increased the *Tfrc* mRNA level (Fig. 5C and D). However, the protein expression of TFR showed no difference among the four experimental groups (Supplementary Fig. 2). These results indicate that PKM2-activated EVs mainly inhibit cellular iron release and in turn increase macrophage iron accumulation.

To further confirm the relationship between iron concentration and macrophage lipid peroxidation or migration, we used the iron chelating agent DFOM. The increased lipid peroxides in cellular membranes and upregulated levels of the lipid peroxidation products LPO and MDA in RAW264.7 cells by $PKM2^{fl/fl}$-Hcy-EVs could be inhibited by pretreatment with DFOM (Fig. 5E-G). Additionally, pretreatment of macrophages with DFOM significantly inhibited the migration-promoting effect of $PKM2^{fl/fl}$-Hcy-EVs (Fig. 5H). Therefore, T lymphocyte-derived EVs facilitate the accumulation of iron and then promote macrophage lipid peroxidation and migration via PKM2.

3.6. PUFA-containing phospholipids encapsulated in EVs from PKM2-activated T lymphocytes may provide substrates for lipid peroxidation in target macrophages

Phospholipids containing PUFAs are susceptible to lipid peroxidation [37]. EVs released from cells are often enriched in lipids such as sphingomyelin, glycosphingolipids, and phosphatidylserine [38,39]. First, lipidomics analysis of EVs derived from T lymphocytes was performed by HPLC-MS/MS. PCA revealed different lipid metabolite profiles in four EV groups, $PKM2^{fl/fl}$-C-EVs, $PKM2^{fl/fl}$-Hcy-EVs, $LckCrePKM2^{fl/fl}$-C-EVs, and $LckCrePKM2^{fl/fl}$-Hcy-EVs (Fig. 6A). The top 15 classes of phospholipid loadings that differed among the four EV groups were shown based on variable importance in projection (VIP) scores (Fig. 6B). Among these species compositions, most of the lipid species that were highly different belonged to the phosphatidylcholine (PC) and phosphatidylethanolamine (PE) lipid classes. Second, we specifically analyzed the levels of PE- or PC-containing polyunsaturated fatty acids in EVs. The heatmap generated by hierarchical clustering of differentially abundant phospholipids enriched in PUFA components

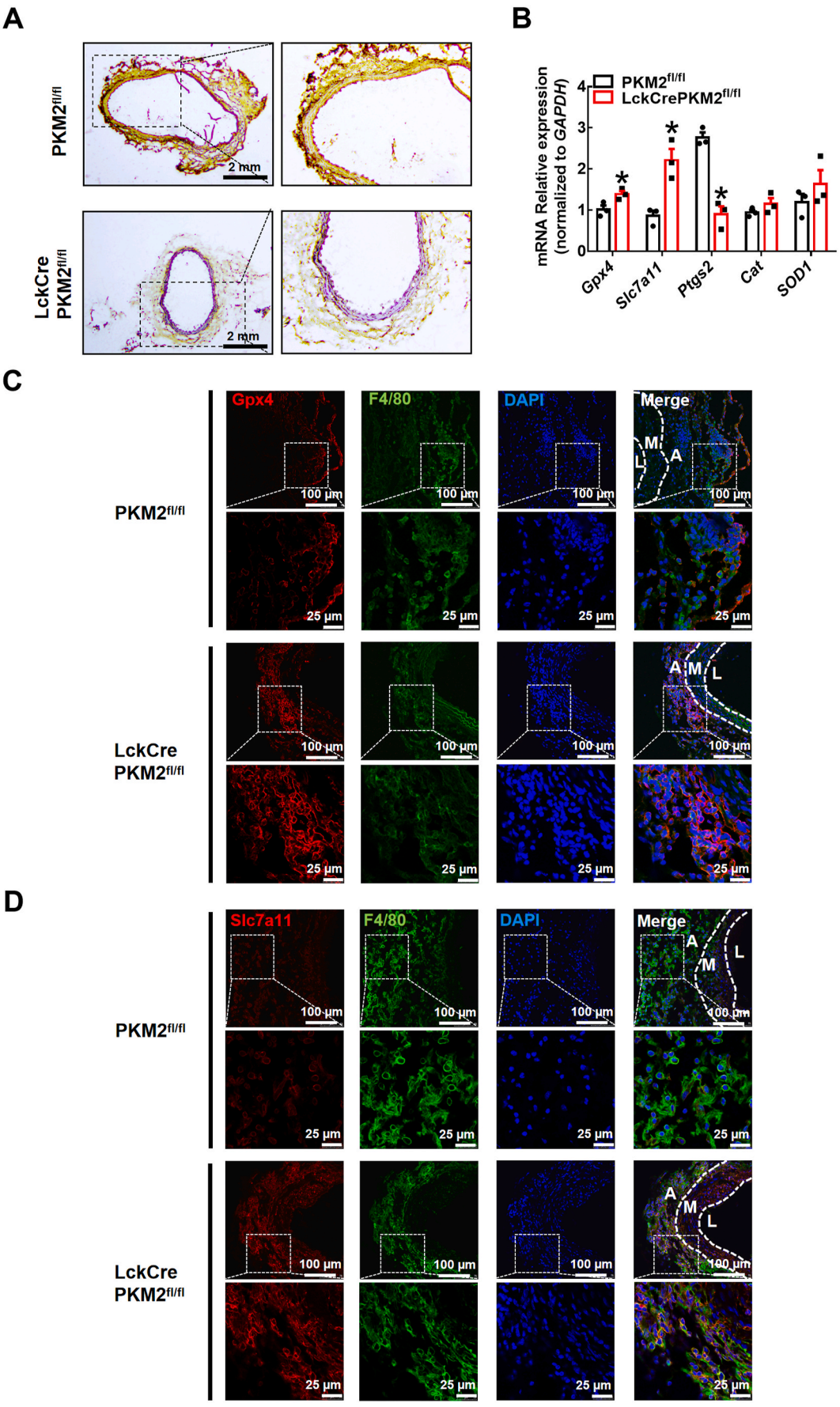

(caption on next page)

Fig. 4. Enhanced macrophage antioxidant effects and inhibited vascular lipid peroxidation in a T lymphocyte-specific PKM2 knockout mouse model with AAA. The infrarenal abdominal aortas of 10-week-old $PKM2^{fl/fl}$ and $LckCrePKM2^{fl/fl}$ mice were treated with elastase for 2 weeks to induce AAA. (A) Representative immunohistochemistry staining for 4-hydroxynonenal (4-HNE) in the infrarenal abdominal aortas of the elastase-treated $PKM2^{fl/fl}$ and $LckCrePKM2^{fl/fl}$ mice. Scale bar, 2 mm. (B) Gene expression levels of *Gpx4*, *Slc7a11*, *Ptgs2*, *SOD1* and *Cat* were measured via qPCR (relative to *GAPDH*) in peritoneal macrophages of the $PKM2^{fl/fl}$ and $LckCrePKM2^{fl/fl}$ mice with AAA. (C) Representative immunofluorescence staining of Gpx4 (red) and macrophages ($F4/80^+$, green) in the infrarenal abdominal aortas. DAPI indicated cell nucleus. Scale bar, 25 μm and 100 μm. (D) Representative immunofluorescence staining of Slc7a11 (red) and macrophages ($F4/80^+$, green) in the infrarenal abdominal aortas. DAPI indicates the cell nucleus. Scale bar, 25 μm and 100 μm. Every microscopy figure is presented as a total view of the field above and a cutout of that field with a high magnification below. A: tunica adventitia; M: tunica medium; L: tunica lumen. n = 3. The data are presented as the mean ± SEM. $^*p < 0.05$, compared with $PKM2^{fl/fl}$. The data were compared using Student's *t*-test. (For interpretation of the references to colour in this figure legend, the reader is referred to the Web version of this article.)

showed marked global inhibition of 16:0–20:4 PE, 16:0–22:6 PE, 18:0–20:4 PE, 18:0–22:6 PE, and 18:0–22:6 PC in the $LckCrePKM2^{fl/fl}$-C-EVs relative to the $PKM2^{fl/fl}$-C-EVs and significantly enhancement in the $PKM2^{fl/fl}$-Hcy-EVs, but complete inhibition in the $LckCrePKM2^{fl/fl}$-Hcy-EVs compared with the $PKM2^{fl/fl}$-Hcy-EVs (Fig. 6C).

To ascertain whether T lymphocyte-derived EVs can be internalized by macrophages, we added Alexa 647-TSG101-labeled EVs to macrophage medium. After 12 h of incubation, Alexa-647-TSG101 was detectable in the cytoplasm of macrophages, implying that EVs can be taken up by these macrophages (Supplementary Fig. 3A). Dynamin 2 is involved in phagocytosis, micropinocytosis, clathrin-associated endocytosis, and caveolin-dependent endocytosis, which are possible mechanisms for EV uptake [40]. Inhibition of dynamin by Dynasore has been reported to block EV internalization in phagocytic cells [41]. Here, we found that migratory inhibition by Dynasore itself showed a dose-dependent effect ranging from 0 to 80 μmol/L, and 20 μmol/L Dynasore did not have this effect (Supplementary Fig. 3B). Therefore, 20 μmol/L Dynasore was chosen for the subsequent experiments.

The remarkable iron accumulation (Fig. 6D) and lipid peroxidation (Fig. 6E-G; Supplementary Fig. 3C) effects and inhibitory effects on the antioxidant capacity (Fig. 6H and I) of $PKM2^{fl/fl}$-Hcy-EVs on RAW264.7 cells were completely diminished by the Dynasore pretreatment. In addition, Transwell migration assays confirmed that the $PKM2^{fl/fl}$-Hcy-EVs promoted macrophage migration, and this effect was also diminished by the Dynasore pretreatment (Fig. 6J). Therefore, EVs from PKM2-activated T lymphocytes encapsulate more phospholipids containing polyunsaturated fatty acids, which may be taken up by macrophages and subsequently provide abundant substrates for lipid peroxidation in target macrophages.

3.7. EVs from AAA patient plasma promote iron accumulation, lipid peroxidation, and migration of macrophages

To confirm whether T lymphocyte PKM2 is associated with pathogenesis and progression in subjects with clinical AAA, we randomly selected seven AAA patients and eight control subjects. Representative computed tomography angiography (CTA) photographs of a patient diagnosed with AAA were shown as Fig. 7A. Preliminary data showed that the expression of PKM2 in T lymphocytes was significantly increased in the AAA patients compared with the control subjects by staining peripheral blood mononuclear cells (PBMCs) isolated from human plasma (Fig. 7B). In addition, no significant differences between the AAA patients and the control subjects were observed in terms of age, sex, smoking habits, history of cardiovascular events, stroke, cancer, diabetes, hypercholesteremia, or hypertension (Supplementary Table 1).

Subsequently, we cultured EVs isolated from AAA patient plasma (PEVs-AAA) or control plasma (PEVs-control) with THP-1 cells for 24 h. The data showed that PEVs-AAA significantly enhanced intracellular Fe^{2+} levels (Fig. 7C), lipid peroxides (Fig. 7D), and lipid peroxidation products LPO (Fig. 7E) and MDA (Fig. 7F) contents in THP-1 cells. Furthermore, pretreatment of THP-1 cells with an inhibitor of lipid peroxidation Fer-1 or the iron chelating agent DFOM markedly inhibited the migration-promoting effect of PEVs-AAA but had no effect on cells incubated with PEVs-control (Fig. 7G). Together with the related data from the animal model above, these data indicate that enhanced T lymphocyte PKM2 contributes to the pathogenesis of aneurysm development through EV secretion to promote macrophage iron accumulation and lipid peroxidation and then facilitate their migration into vascular lesions.

3.8. The sphingomyelinase inhibitor GW4869 ameliorates elastase-induced AAA development in mice

Recent studies have shown that EVs, with unknown cell sources, are detected in the adventitia of aneurysmal tissues obtained from humans and mice with calcium phosphate ($CaPO_4$)-induced AAA [18,42], but the association between EVs and AAA is still unclear. Here, we evaluated whether EVs, especially exosomes, are involved in AAA development *in vivo* by intraperitoneally administering the exosome inhibitor GW4869. Protein concentrations in EVs isolated from plasma were measured. The results showed that circulating EV levels were increased in the elastase-induced AAA group injected intraperitoneally with saline with 2.5% dimethylsulfoxide (AAA + vehicle), and this effect was strikingly inhibited by GW4869 treatment (AAA + GW4869) (Supplementary Table 2). Aortas treated with elastase *in vivo* showed a significant increase in aortic expansion after 14 days compared with that of the sham group (diameter 1.153 ± 0.037 mm in the sham group vs. 2.391 ± 0.133 mm in the AAA + vehicle group; Fig. 8A). Injection of GW4869 significantly mitigated elastase-induced AAA expansion (diameter 2.391 ± 0.133 mm in AAA + vehicle group vs. 1.569 ± 0.072 mm in AAA + GW4869 group; Fig. 8A). The incidence of elastase-induced AAA in the solvent control group (AAA + vehicle) was 100% (8/8), while it was decreased dramatically in the mice intraperitoneally injected with GW4869 (42.86%, 3/7; Fig. 8B). Additionally, Verhoef-Van Gieson staining showed that the severity of elastin degradation was lower in the AAA + GW4869 groups than in the AAA + vehicle group (Fig. 8C). Immunofluorescence staining revealed that MMP9 and MMP2 levels were elevated in elastase-treated aortas, but they were attenuated by GW4869 compared with that of the AAA + vehicle group (Fig. 8D).

To further verify the effects of EVs on macrophage infiltration in AAA, we performed immunofluorescence staining of F4/80 (macrophage marker) in the different experimental groups. The data showed increased expression of F4/80 in the adventitia of the elastase-induced aortas, which was alleviated after intraperitoneal GW4869 injection (Fig. 8E). To verify the inhibitory effects of GW4869 on macrophage migration in murine AAA *ex vivo*, we collected peritoneal macrophages in different experimental groups and examined their migratory activity by a Transwell experimental system with MCP-1 in the lower chamber. The data demonstrated that peritoneal macrophage migration in mice with elastase-induced AAA was efficiently promoted. However, upon intraperitoneal administration of GW4869, cell migration was drastically inhibited (Fig. 8F). Taken together, these data imply that EVs, likely exosomes, are involved in elastase-induced AAA progression and simultaneously increase macrophage migration.

In summary, this study provides evidence showing that the PUFA-containing PL-filled EVs secreted from PKM2-activated T lymphocytes may provide abundant substrates and promote the target macrophage iron-dependent lipid peroxidation, subsequently promoting their

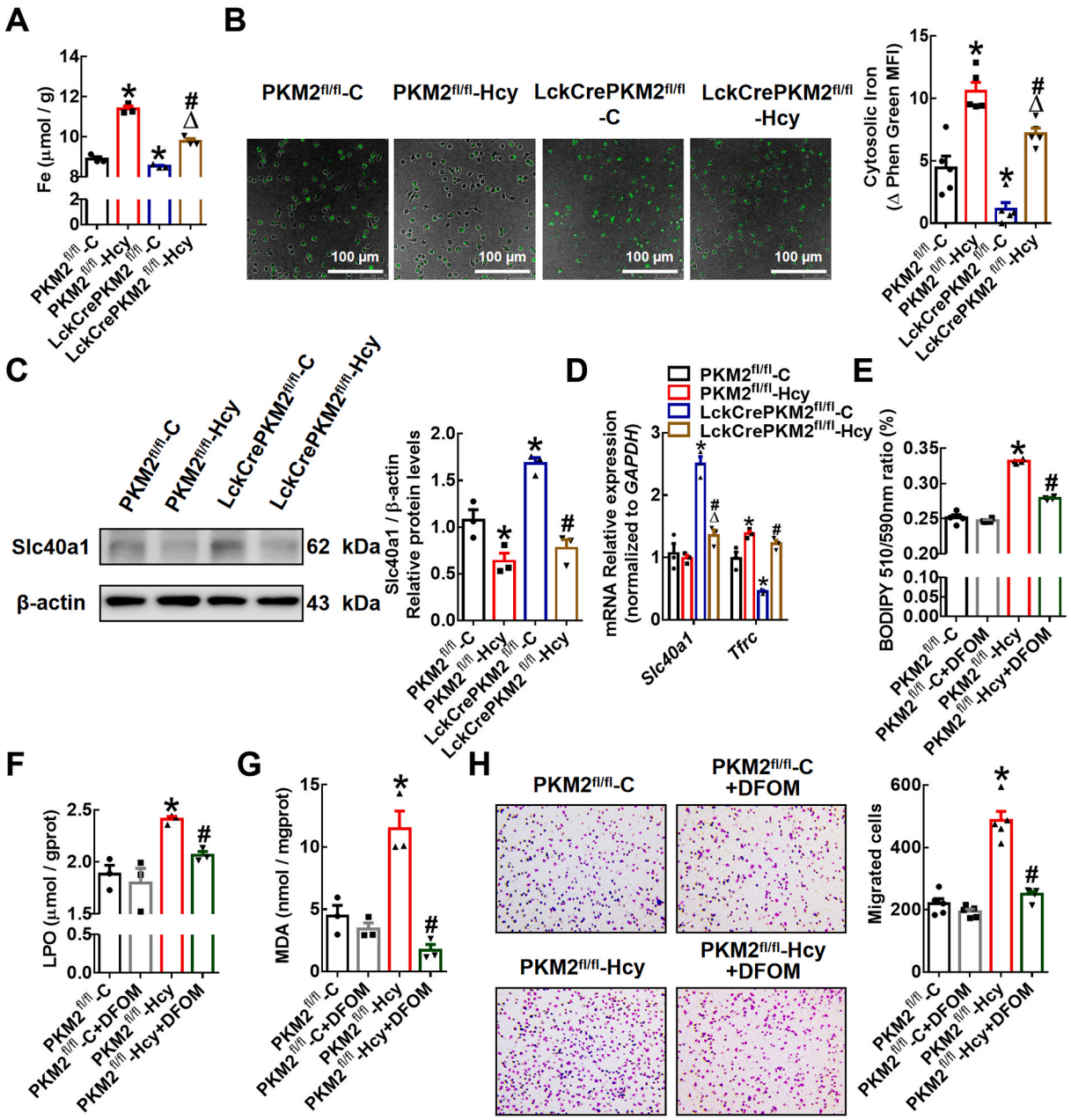

Fig. 5. Extracellular vesicles derived from T lymphocytes promote iron accumulation in macrophages via PKM2.
Equal concentrations (10 μg/mL) of EVs from the PKM2$^{fl/fl}$-C, PKM2$^{fl/fl}$-Hcy, LckCrePKM2$^{fl/fl}$-C or LckCrePKM2$^{fl/fl}$-Hcy T lymphocytes cultured with RAW264.7 cells (A, C-D) or peritoneal macrophages (B) for 24 h n = 3–5. (A) Measurement of intracellular iron concentrations in RAW264.7 cells. (B) Free iron levels in peritoneal macrophages were measured by a Phen Green SK probe. As Phen Green fluorescence is quenched by iron, the inverse of fluorescence was plotted for these dyes to represent relative levels of cellular iron. (C) Protein expression and quantification (relative to β-actin) of Slc40a1 were measured via Western blots of RAW264.7 cells after EV treatment for 48 h. (D) Gene expression levels of *Slc40a1* and *Tfrc* were measured via qPCR in RAW264.7 cells at 24 h after treatment with different EVs. RAW264.7 cells pretreated with the iron chelating agent deferoxamine mesylate (DFOM) (10 μmol/L) were further treated with different EVs. Measurements of the intracellular lipid peroxidation levels were made by quantifying oxidized BODIPY-C11 (emission: 590 nm)/reduced BODIPY-C11 (emission: 510 nm) ratio through flow cytometry (E), lipid peroxidation (LPO) analysis (F), and malondialdehyde (MDA) analysis (G) in RAW264.7 cells. Peritoneal macrophages pretreated with DFOM (10 μmol/L) were then treated with various EVs. (H) Representative images of crystal violet staining were captured at 48 h after incubation and quantification of migrated cells. Cells were counted from 5 random microscope fields for each sample in 5 independent experiments. The data are presented as the mean ± SEM. (A–D) *$p < 0.05$, compared with PKM2$^{fl/fl}$-C. #$p < 0.05$, compared with LckCrePKM2$^{fl/fl}$-C. Δ$p<0.05$, compared with PKM2$^{fl/fl}$-Hcy. (E–H) *$p < 0.05$, compared with PKM2$^{fl/fl}$-C. #$p < 0.05$, compared with PKM2$^{fl/fl}$-Hcy. The data were compared using one-way ANOVA followed by Tukey's multiple comparison test. (For interpretation of the references to colour in this figure legend, the reader is referred to the Web version of this article.)

migration and infiltration into the aortic wall and ultimately contributing to AAA development.

4. Discussion

In an elastase-induced AAA model, we provided the first evidence that T lymphocyte-derived EVs target macrophages and mediate AAA pathogenesis via PKM2 activation. Mechanistically, PKM2-activated T

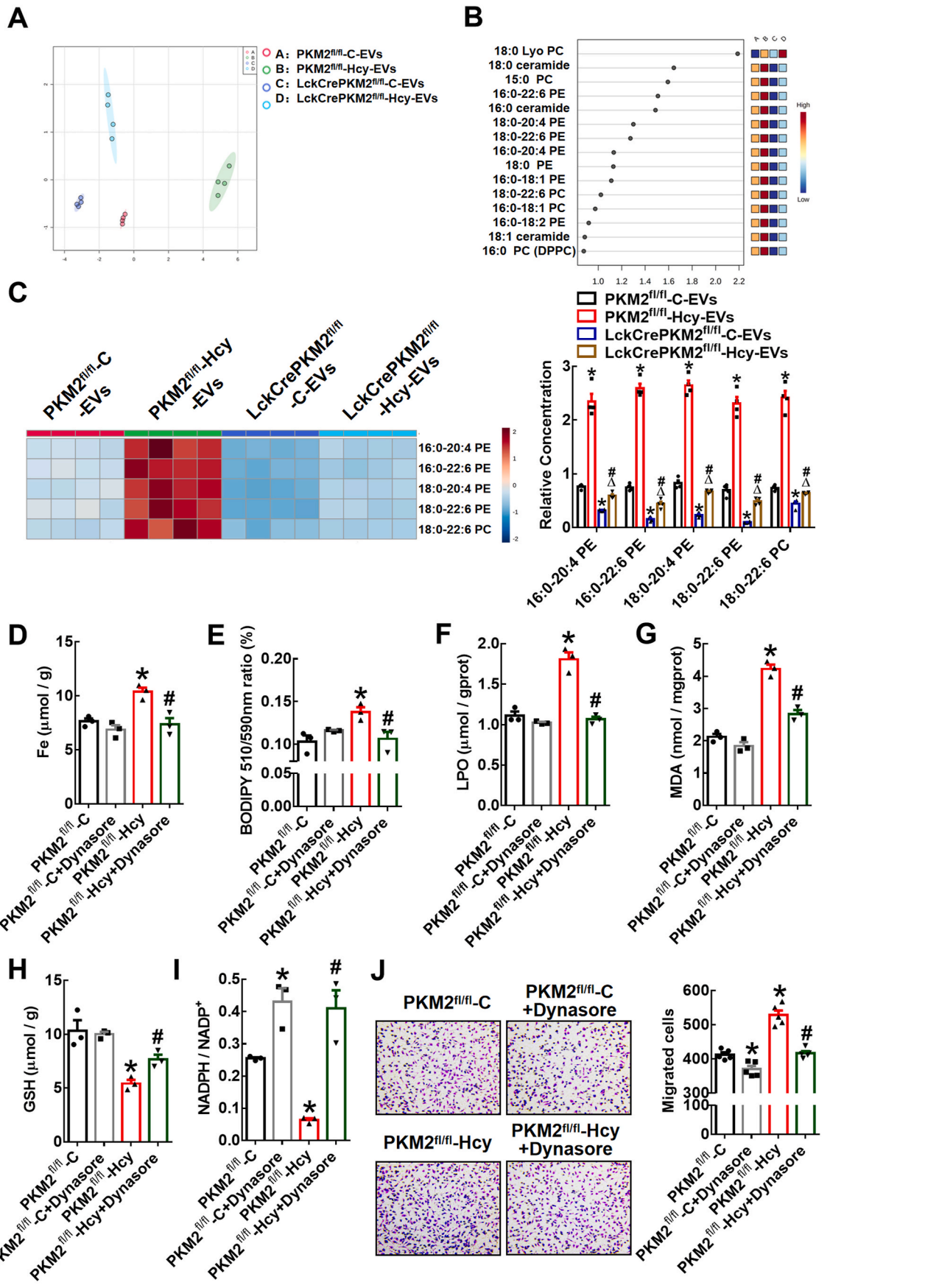

(caption on next page)

Fig. 6. Extracellular vesicles from PKM2-activated T lymphocytes contain more PUFA-containing PLs, which may provide substrates for lipid peroxidation in target macrophages.
HPLC-MS/MS analysis of lipid metabolites in different T lymphocyte-derived EVs isolated from culture supernatants. (A) PCA scatter plot of the lipid metabolites in EVs. (B) VIP scatter plot identified by PCA showing the top 15 lipid metabolites. A: $PKM2^{fl/fl}$-C-EVs, B: $PKM2^{fl/fl}$-Hcy-EVs, C: $LckCrePKM2^{fl/fl}$-C-EVs, D: $LckCrePKM2^{fl/fl}$-Hcy-EVs. (C) Heatmap of changes in the EV phospholipid-containing polyunsaturated fatty acid profile. The relative levels of phospholipids containing polyunsaturated fatty acid metabolites, normalized to EV protein levels, are presented in the right panel. EV protein levels were normalized to lysate total protein. RAW264.7 cells pretreated with Dynasore (20 μmol/L) were further treated with EVs derived from different sources for 24 h (D–I). n = 3–5. (D) Iron concentrations in RAW264.7 cells. (E) Flow cytometric analysis of BODIPY 581/591 C11 in RAW264.7 cells. Quantification of oxidized BODIPY-C11 (emission: 590 nm)/reduced BODIPY-C11 (emission: 510 nm) ratio. Quantification of lipid peroxidation (LPO) (F) and malondialdehyde (MDA) (G) in RAW264.7 cells after incubation with EVs for 24 h. Measuring the concentrations of the antioxidant GSH (H) and NADPH/$NADP^+$ ratio (I) in RAW264.7 cells. Peritoneal macrophages pretreated with Dynasore (20 μmol/L) were then treated with EVs for an additional 48 h. (J) Representative images of crystal violet staining were captured at 48 h after incubation to indicate migrated peritoneal macrophages. Quantification of the migrated cells is shown in the right panel. Cells were counted from 5 random microscopic fields for each sample in 5 independent experiments. The data are presented as the mean ± SEM. (C) $*p < 0.05$, compared with $PKM2^{fl/fl}$-C-EVs. $\#p < 0.05$, compared with $LckCrePKM2^{fl/fl}$-C-EVs. $\Delta p<0.05$, compared with $PKM2^{fl/fl}$-Hcy-EVs. (D–J) $*p < 0.05$, compared with $PKM2^{fl/fl}$-C. $\#p < 0.05$, compared with $PKM2^{fl/fl}$-Hcy. The data were compared using one-way ANOVA followed by Tukey's multiple comparison test. (For interpretation of the references to colour in this figure legend, the reader is referred to the Web version of this article.)

lymphocytes transfer PUFA-containing PL-rich EVs, which may provide substrates for lipid peroxidation in target macrophages, together with intracellular iron accumulation, to promote their migration and subsequently potentiate AAA.

Inflammatory cells accumulated in media and adventitia are essential for AAA [43]. Enhanced glycolysis in the aortic wall is associated with AAA in mice and humans. Although various activated immune cells exhibit a substantial increase in glucose metabolism [44], it has been reported that glycolysis is the preferred type of energy production in macrophages compared to other cell types composing the aorta. The increased expression of GLUT-3, which mediates the uptake of glucose, in macrophages in aneurysmal tissues is associated with macrophage survival and activation and MMP9 activity [25]. Whether glycolysis-related factors other than macrophages contribute to the pathogenesis of aneurysmal tissues need to be determined. In the present study, we found upregulated expression of the glycolytic enzyme PKM2 in T lymphocytes of AAA patients' PBMCs and in infiltrated T lymphocytes of murine AAA vascular lesions. By using our previously successfully created T lymphocyte-specific PKM2 knockout ($LckCrePKM2^{fl/fl}$) mice with much lower glycolysis in T lymphocytes, the present study showed that T lymphocytes with upregulated PKM2 expression mediated elastase-induced murine AAA formation, which extended our understanding of the relationship between T lymphocyte metabolism-related factors and AAA pathogenesis. Recently, it has been reported that PKM2 was elevated in vascular lesions of the thoracic aortic aneurysm and dissection (TAAD) mice and patients, and intraperitoneal injection of PKM2 activator TEPP-46 alleviated TAAD and showed therapeutic potential [45]. These evidences confirmed the pivotal role of PKM2-dependent mechanisms in aortic aneurysm pathogenesis. In our present study, T lymphocyte-specific PKM2 deficiency attenuated AAA by using the specific knock out mice. Therefore, it may be therapeutic for AAA when intervening T-lymphocyte PKM2, however it may be detrimental when inhibiting PKM2 globally yet.

Recently, extracellular vesicles have been shown to play an important role in cardiovascular disease by serving as a mode of intercellular communication [46]. Actually, a higher level of EVs in plasma and aortic wall has been found in patients with AAA compared to the controls, and a consistent trend is also reported in mice with AAA [18,42,47]. Subsequently, EVs have been proven to mediate the interaction between vascular smooth muscle cells or MSCs and macrophages and are linked to AAA [18,19]. In terms of T lymphocyte-derived EVs, preliminary data showed that CD3-positive EVs exist in the adventitia of the aortic wall of a murine model of $CaPO_4$-induced aneurysm [18], while the role of these T lymphocyte-derived EVs in the pathogenesis of AAA remains unknown. In the present study, significantly reduced macrophage infiltration was observed in the aneurysmal aortic wall of $LckCrePKM2^{fl/fl}$ mice with AAA, indicating that the interaction between T lymphocytes and macrophages mediated by PKM2 is associated with the occurrence of AAA. Moreover, we found that intraperitoneal administration of GW4869 to inhibit the generation of EVs weakened elastase-induced AAA progression, confirming the role of EVs in AAA. That GW4869 decreased macrophage infiltration in the aortic wall of the mice with AAA indicated that decreased macrophages in the adventitia of the $LckCrePKM2^{fl/fl}$ mice with AAA may be related to EVs. Together with data from a series of *in vitro* experiments, by using EVs derived from PKM2-deficient or PKM2-activated T lymphocytes to treat macrophages, the present study demonstrated that EVs derived from T lymphocytes contributed to AAA progression via PKM2. In addition, we have reported that HHcy accelerates atherosclerosis via T lymphocyte PKM2-mediated IFN-γ production and cytokine-induced macrophage activation [26,48]. Data from the present study indicated that EVs from PKM2-activated T lymphocytes may also be another potential mechanism to regulate other T lymphocyte-macrophage crosstalk relative cardiovascular diseases, such as atherosclerosis.

Macrophages within the vascular wall have diverse functions, including amplification of the local inflammatory response by secreting proinflammatory cytokines and degradation of extracellular matrix by producing proteases, all of which can promote the occurrence of AAA [49]. Recently published scRNA-seq data confirmed that macrophages are the most numerous immune cells, accounting for 69.04% of infiltrating immune cells in elastase-induced AAA [2]. More importantly, these results also indicated that most infiltrated macrophages in vascular lesions are derived from circulating monocytes. Among the 5 clusters of macrophages singled out in the vascular cells of the elastase-treated AAA model, 3 clusters are derived from peripheral blood monocytes, suggesting the important role of monocyte/macrophage migration in AAA development. In the present study, EVs from the plasma of AAA patients promoted macrophage migration. Alleviated AAA in the $LckCrePKM2^{fl/fl}$ mice was accompanied by decreased macrophages in the vascular adventitia and reduced peritoneal macrophage locomotion. After intraperitoneal administration of GW4869, peritoneal macrophage migration was drastically inhibited *ex vivo*. All this evidence confirmed the pivotal role of macrophage migration in AAA pathogenesis. In addition, it has been reported that macrophage infiltration in the blood vessel wall is regulated by mesenchymal stem cell-derived EVs [19]. Here, we provided evidence to show another new potential source of EVs from PKM2-activated T lymphocytes to promote AAA by regulating macrophage migration.

Oxidative stress is related to the AAA severity [50]. Serum peroxidation contents are found to differ among AAA cases, and the concentration of lipid peroxidation products can be used to predict disease severity and serve as a candidate biomarker for the diagnosis and accurate identification of increased risks of AAA rupture in patients [10]. Human aneurysmal abdominal aortic levels of lipid peroxidation are also determined [51]. However, which cell types exhibit increased lipid peroxidation in local AAA vessels is still unknown. Although macrophages contribute to oxidative stress by producing reactive oxygen species, O_2^- and other oxidants, such as hydrogen peroxide, and then

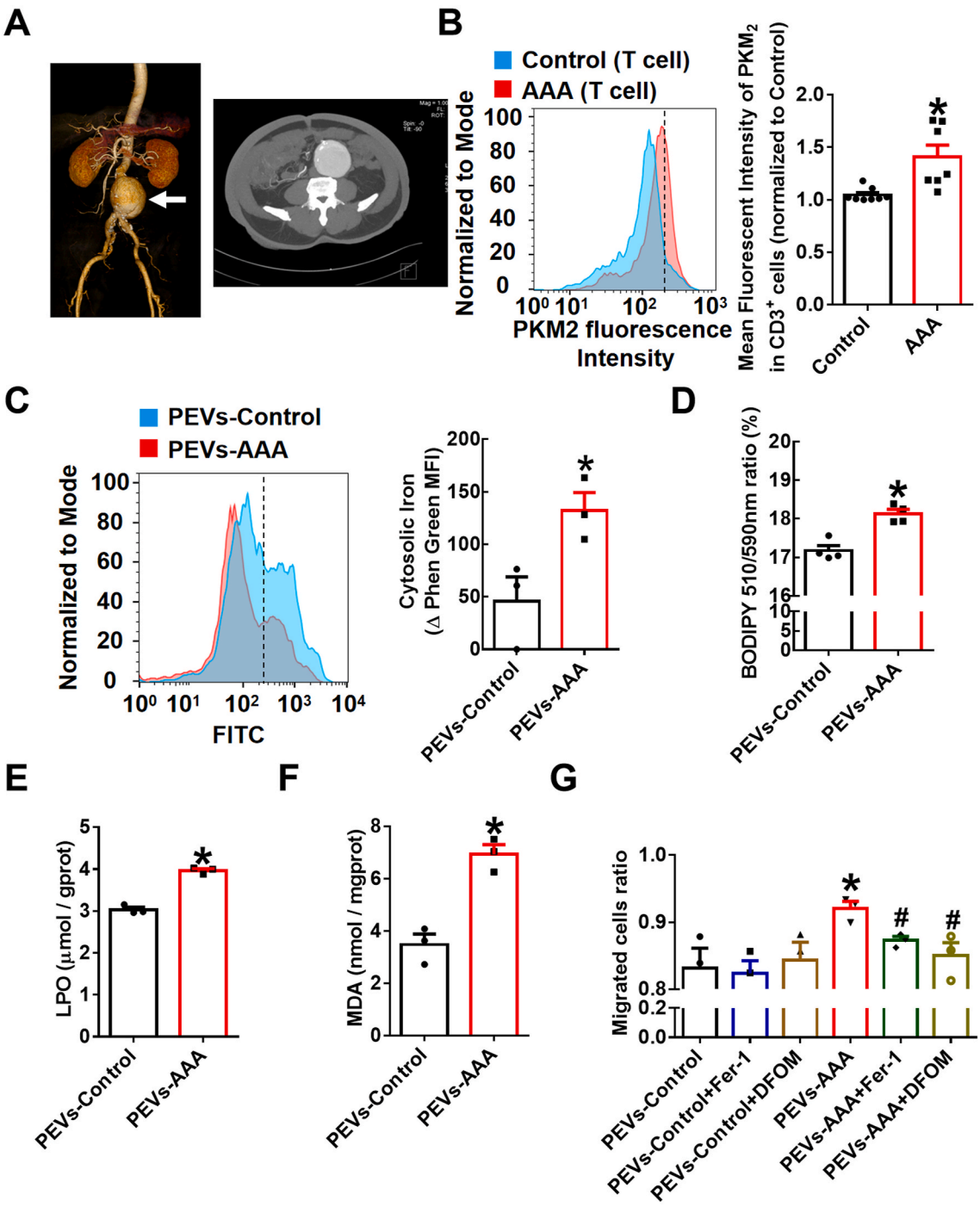

Fig. 7. Extracellular vesicles from AAA patient plasma promote iron accumulation, lipid peroxidation and migration of macrophages.
(A) Representative computed tomography angiography (CTA) photographs of patients diagnosed with AAA. (B) Peripheral blood mononuclear cells (PBMCs) of AAA patients (n = 7) and control subjects (n = 8) were stained with fluorescently conjugated anti-CD3 and anti-PKM2 pAbs and then analyzed by flow cytometry. Quantification of PKM2 in T lymphocytes is shown in the right panel. Equal concentrations (20 μg/mL) of EVs isolated from AAA patient plasma (PEVs-AAA) or control plasma (PEVs-control) were cultured with THP-1 cells for 24 h n = 3–4. (C) Intracellular free iron levels were measured by a Phen Green SK probe. Quantification of the intracellular free iron level, which is inversely proportional to the Phen Green fluorescence intensity. Quantification of the oxidized BODIPY-C11 (emission: 590 nm)/reduced BODIPY-C11 (emission: 510 nm) ratio through flow cytometric analysis (D), lipid peroxidation (LPO) (E) and malondialdehyde (MDA) (F) in THP-1 cells. (G) Transwell migration assays of the PEV (20 μg/mL)-treated THP-1 cells in the upper chamber toward MCP-1 (20 ng/mL) in the lower chamber with or without the lipid peroxidation inhibitor Fer-1 (5 μmol/L) or the iron chelating agent DFOM (20 μmol/L). After 48 h of incubation, cells that had migrated to the bottom chamber or were still in the upper chamber were quantified by flow cytometry, and the migrated cell ratio was calculated (n = 3). The data are presented as the mean ± SEM. (B) *$p < 0.05$, compared with the control. (C–F) *$p < 0.05$, compared with PEVs-control. (G) *$p < 0.05$, compared with PEVs-control. #$p < 0.05$, compared with PEVs-AAA. The data were compared using Student's *t*-test (B–F) or one-way ANOVA followed by Tukey's multiple comparison test (G). (For interpretation of the references to colour in this figure legend, the reader is referred to the Web version of this article.)

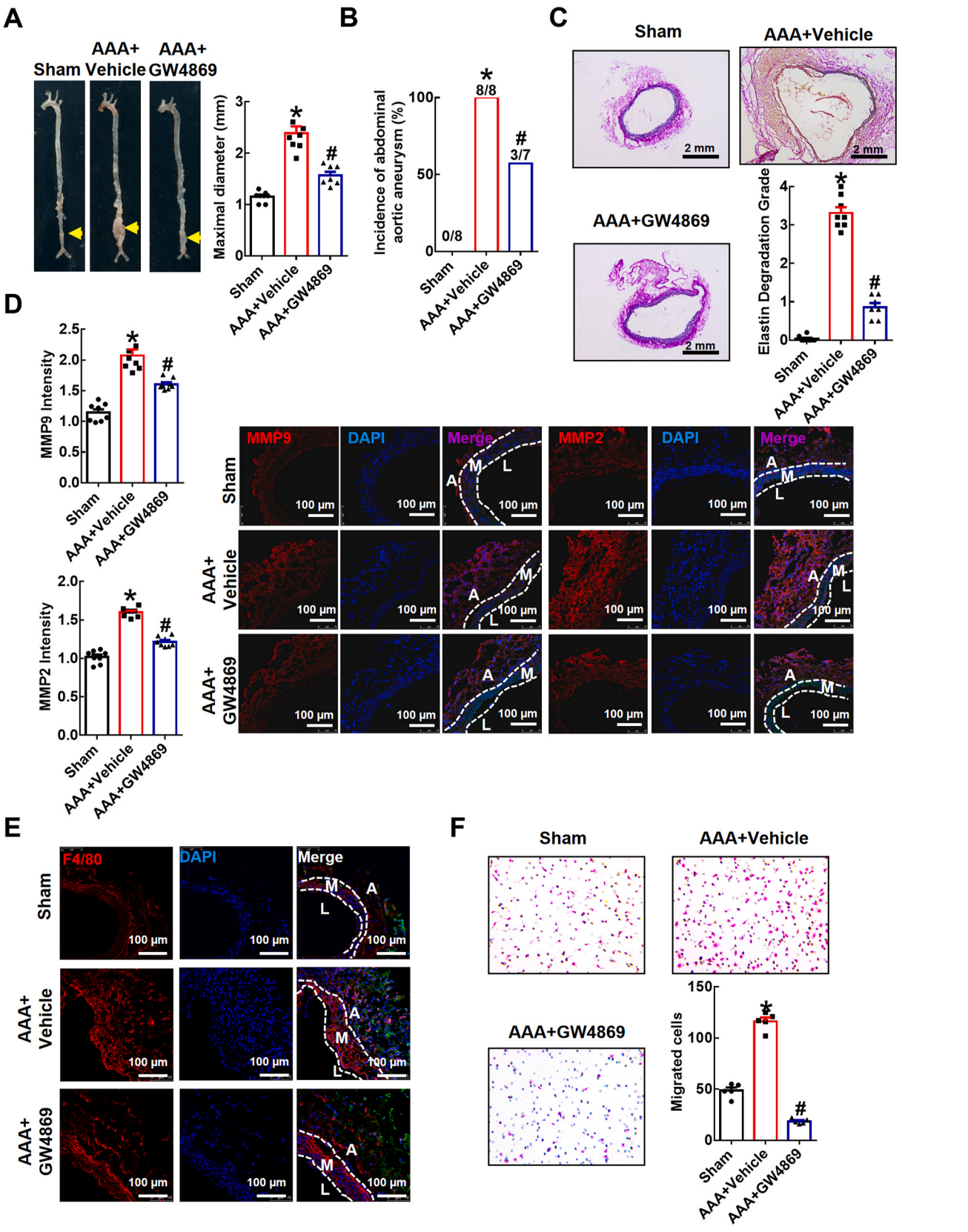

(caption on next page)

Fig. 8. The sphingomyelinase inhibitor GW4869 attenuates elastase-induced AAA in mice.
The infrarenal abdominal aortas of 10-week-old C57BL/6J
mice were treated with elastase for 2 weeks to induce AAA. Mice were injected intraperitoneally once daily with GW4869 (1.25 mg/kg, dissolved in saline with 2.5% dimethylsulfoxide) (AAA +
GW4869) or saline with 2.5% dimethylsulfoxide (AAA +vehicle) 7 days prior to elastase-induced AAA for a total of 21 injections. (A) Representative photographs and quantification of maximal diameters of infrarenal abdominal aortas in the sham mice and the elastase-induced mice with AAA with or without GW4869 treatment. (B) Incidences of AAA. (C) Representative Verhoef-Van Gieson staining and statistical analysis of elastin degradation in the infrarenal abdominal aortas. Scale bar, 2 mm. (D) Quantification of MMP9 and MMP2 expression by fluorescence intensity. Representative immunofluorescence staining of MMP9 and MMP2 in aortic tissue is shown in the right panel. DAPI indicates cell nucleus. Scale bar, 100 μm. A: tunica adventitia; M: tunica medium; L: tunica lumen. (E) Representative immunofluorescence staining of macrophages (anti-F4/80 antibody, red) in the infrarenal abdominal aortas. DAPI indicates the cell nucleus. Scale bar, 100 μm. A: tunica adventitia; M: tunica medium; L: tunica lumen. (F) Representative images of crystal violet staining and quantitative numbers of migrated peritoneal macrophages after incubation for 48 h in a Transwell experimental system. Cells were counted from 5 random microscope fields for each sample in 5 independent experiments. The data are presented as the mean ± SEM. $*p < 0.05$, compared with the sham. $\#p < 0.05$, compared with AAA + vehicle. The data were compared using one-way ANOVA followed by Tukey's multiple comparison test or Fisher's exact test (B). Sham, n = 8; AAA + vehicle, n = 8; AAA + GW4869, n = 7. (For interpretation of the references to colour in this figure legend, the reader is referred to the Web version of this article.)

promote the occurrence of AAA, it is unclear whether and how lipid peroxidation is involved in macrophage function. In our study, EVs derived from PKM2-activated T lymphocytes inhibited the antioxidant effects of GSH and NADPH in macrophages and then promoted lipid peroxidation, increased intracellular LPO and MDA accumulation and macrophage migration, consequently induced AAA. Erastin, an inhibitor of system Xc-activity, enhances lipid peroxidation [52], and it promoted macrophage migration showed in our study. More importantly, EVs isolated from AAA patient plasma significantly promoted macrophage lipid peroxidation and migration, and the migration-promoting effect could be inhibited by the lipid peroxidation inhibitor Fer-1. In the cancer research field, conversely, many studies have suggested that inducing cancer cell lipid peroxidation is a prospective therapeutic strategy for various carcinomas by inhibiting cancer cell migration and proliferation [53,54]. This discrepancy may be due to the different cell types and cellular and organizational microenvironments. However, it is still confirmed about the exact mechanisms for lipid peroxidation to induce macrophage migration.

Although iron is an essential element for various proteins that maintain physiological function, excess local iron retention damages tissue and induces AAA formation by oxidative stress and inflammation [11,55]. Compared with those in non-AAA walls, the iron transport protein Tfr1 is increased and iron is accumulated in human and angiotensin II-induced murine AAA walls [11]. All this evidence confirms that iron deposition positively correlates with AAA severity. However, which cell types are possible contributors to iron disorder and the potential mechanisms are still unclear. Herein, we demonstrated that PKM2-activated T lymphocytes released EVs to promote macrophage iron accumulation by inhibiting iron export, subsequently increase macrophage migration. RAW264.7 cells pretreated with the iron chelating agent DFOM inhibited the promotion of macrophage migration induced by PKM2-activated T lymphocyte-derived EVs. Conversely, EVs derived from PKM2-null T lymphocytes promoted iron efflux by increasing Slc40a1 to inhibit macrophage iron accumulation. Importantly, EVs isolated from AAA patient plasma promoted macrophage iron accumulation, and their migration-promoting effect could be inhibited by DFOM. A differential proteomic study based on human plasma-derived EVs showed that exosomes from AAA patients upregulate the levels of ferritin, a protein involved in iron storage [47]. Although our study confirmed that PKM2-mediated T lymphocyte-derived EVs promoted target macrophage iron accumulation, which was mostly associated with decreased iron effluxion, whether elevated PKM2 in T lymphocytes during AAA affects iron metabolic components of EVs to further regulate target cell function needs to be determined. To date, there have been two reports about the relationship between iron and macrophage migration. One report showed that increased intracellular iron and lipid peroxidation in splenic red pulp macrophages (RPMs) caused by erythrophagocytosis leads to increased chemokine expression, which signals monocyte migration from bone marrow to spleen [56]. The other study showed that the H67D variant of HFE, a hemochromatosis gene, influences iron absorption by modulating the expression of hepcidin, increases the cellular iron concentration in macrophages and inhibits cellular migration [57]. It is likely that the regulation of iron metabolism may exert different effects on macrophage migration in various experimental or pathological systems.

Recently, the term ferroptosis is coined to describe a type of cell death distinct from other kinds of regulated cell death [58]. The main feature of the ferroptotic death is the iron-dependent accumulation of lipid-based reactive oxygen species. Although our study confirmed that PKM2-mediated T lymphocyte-derived EVs promoted target macrophage iron accumulation and lipid peroxidation and subsequently increased cell migration, these EVs had no significant effect on cell death. After continued coculture with four types of EVs for 24 h or pretreatment of RAW264.7 cells with Fer-1 or DFOM followed by incubation with $PKM2^{fl/fl}$-Hcy-EVs, the proportions of live cells between different groups showed no striking difference and were typically greater than 80% (Supplementary Fig. 4). This result indicated that cell death may not be the only outcome of the intracellular iron accumulation and lipid peroxidation, and cell migration or other processes could occur. The main effect of the iron-lipid peroxidation axis in our study is regulating macrophage locomotion and then driving AAA progression.

Extracellular vesicles contain diverse biomolecules, such as lipids, proteins, and nucleic acids, which derived from the donor cells. Herein, lipidomics analysis showed that EVs from PKM2-activated T lymphocytes contained much more phospholipids enriched with polyunsaturated fatty acids, such as 16:0–20:4 PE, 16:0–22:6 PE, 18:0–20:4 PE, 18:0–22:6 PE, and 18:0–22:6 PC, all of which are intracellular lipid peroxidation substrates. T lymphocyte-derived EVs could enter the target cells. Inhibition of endocytosis with the pharmacological inhibitor Dynasore significantly attenuated EV-induced macrophage iron storage, lipid peroxidation and migration, indicating that EVs from PKM2-activated T lymphocytes may enter macrophages to provide abundant substrates for lipid peroxidation in these target cells. However, the exact mechanisms by which T lymphocyte PKM2 alters the composition of EVs and whether and which phospholipids predominantly affect macrophage migration need to be further investigated.

In summary, our study reveals that T lymphocyte-derived EVs enriched with PUFA-containing PLs promote macrophage migration by promoting iron accumulation and lipid peroxidation and then aggravating AAA via PKM2, from the cell-cell crosstalk and metabolic perspectives. This finding also suggests that the iron-lipid peroxidation axis may be a potential intervention target for the treatment of activated macrophage-related vascular inflammatory diseases.

Funding

This study was funded by the National Natural Science Foundation of China (Nos. 91939105, 82170476, and 81770445) and the Natural Science Foundation of Beijing, China (No. M21008).

Author contributions

J.F. and X.W. designed and supervised the research; G.D. performed the research, analyzed the data, made the figures and wrote the manuscript; T.L. G.Y., and X.L. designed, provided the human clinical samples and assisted in the research; D.Y., X.D., J.Y., Y.M., L.H., X.M., Y.S., and B. L. participated in the collection of experimental data.

Declaration of competing interest

None declared.

Appendix A. Supplementary data

Supplementary data to this article can be found online at https://doi.org/10.1016/j.redox.2022.102257.

References

[1] N. Sakalihasani, J.B. Michel, A. Katsargyris, H. Kuivaniemi, J.O. Defraigne, A. Nchimi, J.T. Powell, K. Yoshimura, R. Hultgren, Abdominal aortic aneurysms, Nat. Rev. Dis. Prim. 4 (1) (2018) 34, https://doi.org/10.1038/s41572-018-0030-7.

[2] G. Zhao, H. Lu, Z. Chang, Y. Zhao, T. Zhu, L. Chang, Y. Guo, M.T. Garcia-Barrio, Y. E. Chen, J. Zhang, Single cell RNA sequencing reveals the cellular heterogeneity of aneurysmal infrarenal abdominal aorta, Cardiovasc. Res. 117 (5) (2021) 1402–1416, https://doi.org/10.1093/cvr/cvaa214.

[3] C.S. Moran, R.J. Jose, J.V. Moxon, A. Roomberg, P.E. Norman, C. Rush, H. Körner, J. Golledge, Everolimus limits aortic aneurysm in the apolipoprotein E-deficient mouse by downregulating C-C chemokine receptor 2 positive monocytes, Arterioscler. Thromb. Vasc. Biol. 33 (4) (2013) 814–821, https://doi.org/10.1161/ATVBAHA.112.301006.

[4] V. de Waard, I. Bot, S.C. de Jager, S. Talib, K. Egashira, M.R. de Vries, P.H. Quax, E. A. Biessen, T.J. van Berkel, Systemic MCP1/CCR2 blockade and leukocyte specific MCP1/CCR2 inhibition affect aortic aneurysm formation differently, Atherosclerosis 211 (1) (2010) 84–89, https://doi.org/10.1016/j.atherosclerosis.2010.01.042.

[5] D. Ma, B. Zheng, T. Suzuki, R. Zhang, C. Jiang, D. Bai, W. Yin, Z. Yang, X. Zhang, L. Hou, H. Zhan, J.K. Wen, Inhibition of KLF5-Myo9b-RhoA pathway-mediated podosome formation in macrophages ameliorates abdominal aortic aneurysm, Circ. Res. 120 (5) (2017) 799–815, https://doi.org/10.1161/CIRCRESAHA.116.310367.

[6] E. Aflaki, N.A. Balenga, P. Luschnig-Schratl, H. Wolinski, S. Povoden, P. G. Chandak, J.G. Bogner-Strauss, S. Eder, V. Konya, S.D. Kohlwein, A. Heinemann, D. Kratky, Impaired Rho GTPase activation abrogates cell polarization and migration in macrophages with defective lipolysis, Cell. Mol. Life Sci. 68 (23) (2011) 3933–3947, https://doi.org/10.1007/s00018-011-0688-4.

[7] J. Xu, J. Yang, A. Nyga, M. Ehteramyan, A. Moraga, Y. Wu, L. Zeng, M.M. Knight, J. C. Shelton, Cobalt (II) ions and nanoparticles induce macrophage retention by ROS-mediated down-regulation of RhoA expression, Acta Biomater. 72 (2018) 434–446, https://doi.org/10.1016/j.actbio.2018.03.054.

[8] B. Sun, F. Li, S. Lai, X. Zhang, H. Wang, Y. Li, W. Wang, Y. Chen, B. Liu, Y. Zheng, Inhibition of CXCR2 alleviates the development of abdominal aortic aneurysm in ApoE$^{-/-}$ mice, Acta Cir. Bras. 36 (1) (2021), e360105, https://doi.org/10.1590/ACB360105.

[9] S. Zhong, L. Li, X. Shen, Q. Li, W. Xu, X. Wang, Y. Tao, H. Yin, An update on lipid oxidation and inflammation in cardiovascular diseases, Free Radic. Biol. Med. 144 (2019) 266–278, https://doi.org/10.1016/j.freeradbiomed.2019.03.036.

[10] F. Shi, C.C. Ma, C. Ji, M. Li, X. Liu, Y.S. Han, Serum lipid oxidative stress products as risk factors are the candidate predictive biomarkers for human abdominal aortic aneurysms, Clin. Appl. Thromb. Hemost. 26 (2020), https://doi.org/10.1177/1076029620932226.

[11] H. Sawada, H. Hao, Y. Naito, M. Oboshi, S. Hirotani, M. Mitsuno, Y. Miyamoto, S. Hirota, T. Masuyama, Aortic iron overload with oxidative stress and inflammation in human and murine abdominal aortic aneurysm, Arterioscler. Thromb. Vasc. Biol. 35 (6) (2015) 1507–1514, https://doi.org/10.1161/ATVBAHA.115.305586.

[12] L. Boytard, R. Spear, G. Chinetti-Gbaguidi, A.E. Acosta-Martin, J. Vanhoutte, N. Lamblin, B. Staels, P. Amouyel, S. Haulon, F. Pinet, Role of proinflammatory CD68(+) mannose receptor(-) macrophages in peroxiredoxin-1 expression and in abdominal aortic aneurysms in humans, Arterioscler. Thromb. Vasc. Biol. 33 (2) (2013) 431–438, https://doi.org/10.1161/ATVBAHA.112.300663.

[13] C. Kruger, S.J. Burke, J.J. Collier, T.T. Nguyen, J.M. Salbaum, K. Stadler, Lipid peroxidation regulates podocyte migration and cytoskeletal structure through redox sensitive RhoA signaling, Redox Biol. 16 (2018) 248–254, https://doi.org/10.1016/j.redox.2018.02.024.

[14] P. Chen, Q. Wu, J. Feng, L. Yan, Y. Sun, S. Liu, Y. Xiang, M. Zhang, T. Pan, X. Chen, T. Duan, L. Zhai, B. Zhai, W. Wang, R. Zhang, B. Chen, X. Han, Y. Li, L. Chen, Y. Liu, X. Huang, T. Jin, W. Zhang, H. Luo, X. Chen, Y. Li, Q. Li, G. Li, Q. Zhang, L. Zhuo, Z. Yang, H. Tang, T. Xie, X. Ouyang, X. Sui, Erianin, a novel dibenzyl compound in Dendrobium extract, inhibits lung cancer cell growth and migration via calcium/calmodulin-dependent ferroptosis, Signal Transduct Target Ther 5 (1) (2020) 51, https://doi.org/10.1038/s41392-020-0149-3.

[15] G. van Niel, G. D'Angelo, G. Raposo, Shedding light on the cell biology of extracellular vesicles, Nat. Rev. Mol. Cell Biol. 19 (4) (2018) 213–228, https://doi.org/10.1038/nrm.2017.125.

[16] C.M. Boulanger, X. Loyer, P.E. Rautou, N. Amabile, Extracellular vesicles in coronary artery disease, Nat. Rev. Cardiol. 14 (5) (2017) 259–272, https://doi.org/10.1038/nrcardio.2017.7.

[17] M. Quaglia, S. Dellepiane, G. Guglielmetti, G. Merlotti, G. Castellano, V. Cantaluppi, Extracellular vesicles as mediators of cellular crosstalk between immune system and kidney graft, Front. Immunol. 11 (2020) 74, https://doi.org/10.3389/fimmu.2020.00074.

[18] Y.D. Wang, L.L. Jia, Y. Xie, Z.J. Cai, Z.J. Liu, J. Shen, Y. Lu, Y.P. Wang, S.A. Su, Y. K. Ma, M.X. Xiang, Involvement of macrophage-derived exosomes in abdominal aortic aneurysms development, Atherosclerosis 289 (2019) 64–72, https://doi.org/10.1016/j.atherosclerosis.2019.08.016.

[19] M. Spinosa, G. Lu, G. Su, S.V. Bontha, R. Gehrau, M.D. Salmon, J.R. Smith, M. L. Weiss, V.R. Mas, G.R. Upchurch Jr., A.K. Sharma, Human mesenchymal stromal cell-derived extracellular vesicles attenuate aortic aneurysm formation and macrophage activation via microRNA-147, Faseb. J. (2018), fj201701138RR, https://doi.org/10.1096/fj.201701138RR.

[20] S. Mellak, H. Ait-Oufella, B. Esposito, X. Loyer, M. Poirier, T.F. Tedder, A. Tedgui, Z. Mallat, S. Potteaux, Angiotensin II mobilizes spleen monocytes to promote the development of abdominal aortic aneurysm in Apoe$^{-/-}$ mice, Arterioscler. Thromb. Vasc. Biol. 35 (2) (2015) 378–388, https://doi.org/10.1161/ATVBAHA.114.304389.

[21] A. Sagan, T.P. Mikolajczyk, W. Mrowiecki, N. MacRitchie, K. Daly, A. Meldrum, S. Migliarino, C. Delles, K. Urbanski, G. Filip, B. Kapelak, P. Maffia, R. Touyz, T. J. Guzik, T cells are dominant population in human abdominal aortic aneurysms and their infiltration in the perivascular tissue correlates with disease severity, Front. Immunol. 10 (2019) 1979, https://doi.org/10.3389/fimmu.2019.01979.

[22] J. Yang, G.H. Dang, S.L. Lu, H.Y. Liu, X.L. Ma, L.L. Han, J.C. Deng, Y.T. Miao, X. P. Li, F.Y. Shao, C.T. Jiang, Q.B. Xu, X. Wang, J. Feng, T-cell-derived extracellular vesicles regulate B-cell IgG production via pyruvate kinase muscle isozyme 2, Faseb. J. 33 (11) (2019) 12780–12799, https://doi.org/10.1096/fj.201900863R.

[23] C. Marbaniang, L. Kma, Dysregulation of glucose metabolism by oncogenes and tumor suppressors in cancer cells, Asian Pac. J. Cancer Prev. APJCP 19 (9) (2018) 2377–2390, https://doi.org/10.22034/APJCP.2018.19.9.2377.

[24] J.C. Deng, S.L. Lu, H.Y. Liu, B. Liu, C.T. Jiang, Q.B. Xu, J. Feng, X. Wang, Homocysteine activates B cells via regulating PKM2-dependent metabolic reprogramming, J. Immunol. 198 (1) (2017) 170–183, https://doi.org/10.4049/jimmunol.1600613.

[25] T. Tsuruda, K. Hatakeyama, S. Nagamachi, Y. Sekita, S. Sakamoto, G.J. Endo, M. Nishimura, M. Matsuyama, K. Yoshimura, Y. Sato, T. Onitsuka, T. Imamura, Y. Asada, K. Kitamura, Inhibition of development of abdominal aortic aneurysm by glycolysis restriction, Arterioscler. Thromb. Vasc. Biol. 32 (6) (2012) 1410–1417, https://doi.org/10.1161/ATVBAHA.111.237065.

[26] S.L. Lu, J.C. Deng, H.Y. Liu, B. Liu, J. Yang, Y.T. Miao, J. Li, N. Wang, C.T. Jiang, Q. B. Xu, X. Wang, J. Feng, PKM2-dependent metabolic reprogramming in CD4(+) T cells is crucial for hyperhomocysteinemia-accelerated atherosclerosis, J Mol Med 96 (6) (2018) 585–600, https://doi.org/10.1007/s00109-018-1645-6.

[27] W. Sun, Y. Pang, Z. Liu, L. Sun, B. Liu, M. Xu, Y. Dong, J. Feng, C. Jiang, W. Kong, X. Wang, Macrophage inflammasome mediates hyperhomocysteinemia-aggravated abdominal aortic aneurysm, J. Mol. Cell. Cardiol. 81 (2015) 96–106, https://doi.org/10.1016/j.yjmcc.2015.02.005.

[28] A. Wanhainen, F. Verzini, I. Van Herzeele, E. Allaire, M. Bown, T. Cohnert, F. Dick, J. van Herwaarden, C. Karkos, M. Koelemay, T. Kolbel, I. Loftus, K. Mani, G. Melissano, J. Powell, Z. Szeberin, G.J. de Borst, N. Chakfe, S. Debus, R. Hinchliffe, S. Kakkos, I. Koncar, P. Kolh, J.S. Lindholt, M. de Vega, F. Vermassen, M. Bjorck, S. Cheng, R. Dalman, L. Davidovic, K. Donas, J. Earnshaw, H. H. Eckstein, J. Golledge, S. Haulon, T. Mastracci, R. Naylor, J.B. Ricco, H. Verhagen, E.G. Comm, Editor's choice - European Society for Vascular Surgery (ESVS) 2019 clinical practice guidelines on the management of abdominal aorto-iliac artery aneurysms, Eur J Vasc Endovasc 57 (1) (2019) 8–93, https://doi.org/10.1016/j.ejvs.2018.09.020.

[29] Y. Miao, Y. Zhao, L. Han, X. Ma, J. Deng, J. Yang, S. Lu, F. Shao, W. Kong, W. Wang, Q. Xu, X. Wang, J. Feng, NSun2 regulates aneurysm formation by promoting autotaxin expression and T cell recruitment, Cell. Mol. Life Sci. 78 (4) (2021) 1709–1727, https://doi.org/10.1007/s00018-020-03607-7.

[30] C.W. Kotze, L.J. Menezes, R. Endozo, A.M. Groves, P.J. Ell, S.W. Yusuf, Increased metabolic activity in abdominal aortic aneurysm detected by 18F-fluorodeoxyglucose (18F-FDG) positron emission tomography/computed tomography (PET/CT), Eur. J. Vasc. Endovasc. Surg. 38 (1) (2009) 93–99, https://doi.org/10.1016/j.ejvs.2008.12.016.

[31] L. Moreira-Costa, A.S. Barros, A.P. Lourenço, A.F. Leite-Moreira, R. Nogueira-Ferreira, V. Thongboonkerd, R. Vitorino, Exosome-derived mediators as potential biomarkers for cardiovascular diseases: a network approach, Proteomes 9 (1) (2021) 8, https://doi.org/10.3390/proteomes9010008.

[32] M. Navas-Madroñal, C. Rodriguez, M. Kassan, J. Fité, J.R. Escudero, L. Cañes, J. Martínez-González, M. Camacho, M. Galán, Enhanced endoplasmic reticulum and mitochondrial stress in abdominal aortic aneurysm, Clin Sci (Lond). 133 (13) (2019) 1421–1438, https://doi.org/10.1042/CS20190399.

[33] M.R. Liu, W.T. Zhu, D.S. Pei, System Xc(-): a key regulatory target of ferroptosis in cancer, Invest. N. Drugs 39 (4) (2021) 1123–1131, https://doi.org/10.1007/s10637-021-01070-0.

[34] K.S. Evonuk, B.J. Baker, R.E. Doyle, C.E. Moseley, C.M. Sestero, B.P. Johnston, P. De Sarno, A. Tang, I. Gembitsky, S.J. Hewett, C.T. Weaver, C. Raman, T. M. DeSilva, Inhibition of system Xc(-) transporter attenuates autoimmune inflammatory demyelination, J. Immunol. 195 (2) (2015) 450–463, https://doi.org/10.4049/jimmunol.1401108.
[35] T. Ganz, Macrophages and iron metabolism, Microbiol. Spectr. 4 (5) (2016), https://doi.org/10.1128/microbiolspec.MCHD-0037-2016.
[36] W. Aerbajinai, M.C. Ghosh, J. Liu, C. Kumkhaek, J. Zhu, K. Chin, T.A. Rouault, G. P. Rodgers, Glia maturation factor-γ regulates murine macrophage iron metabolism and M2 polarization through mitochondrial ROS, Blood Adv 3 (8) (2019) 1211–1225, https://doi.org/10.1182/bloodadvances.2018026070.
[37] A. Catalá, Lipid peroxidation of membrane phospholipids generates hydroxy-alkenals and oxidized phospholipids active in physiological and/or pathological conditions, Chem. Phys. Lipids 157 (1) (2009) 1–11, https://doi.org/10.1016/j.chemphyslip.2008.09.004.
[38] T. Skotland, N.P. Hessvik, K. Sandvig, A. Llorente, Exosomal lipid composition and the role of ether lipids and phosphoinositides in exosome biology, J. Lipid Res. 60 (1) (2019) 9–18, https://doi.org/10.1194/jlr.R084343.
[39] E. Boilard, Extracellular vesicles and their content in bioactive lipid mediators: more than a sack of microRNA, J. Lipid Res. 59 (11) (2018) 2037–2046, https://doi.org/10.1194/jlr.R084640.
[40] L.A. Mulcahy, R.C. Pink, D.R. Carter, Routes and mechanisms of extracellular vesicle uptake, J. Extracell. Vesicles 3 (2014), https://doi.org/10.3402/jev.v3.24641.
[41] D. Feng, W.L. Zhao, Y.Y. Ye, X.C. Bai, R.Q. Liu, L.F. Chang, Q. Zhou, S.F. Sui, Cellular internalization of exosomes occurs through phagocytosis, Traffic 11 (5) (2010) 675–687, https://doi.org/10.1111/j.1600-0854.2010.01041.x.
[42] M. Folkesson, C. Li, S. Frebelius, J. Swedenborg, D. Wagsater, K.J. Williams, P. Eriksson, J. Roy, M.L. Liu, Proteolytically active ADAM10 and ADAM17 carried on membrane microvesicles in human abdominal aortic aneurysms, Thromb. Haemostasis 114 (6) (2015) 1165–1174, https://doi.org/10.1160/TH14-10-0899.
[43] K.D. Rizas, N. Ippagunta, M.D. Tilson 3rd, Immune cells and molecular mediators in the pathogenesis of the abdominal aortic aneurysm, Cardiol. Rev. 17 (5) (2009) 201–210, https://doi.org/10.1097/CRD.0b013e3181b04698.
[44] C.S. Palmer, T. Hussain, G. Duette, T.J. Weller, M. Ostrowski, I. Sada-Ovalle, S. M. Crowe, Regulators of glucose metabolism in CD4(+) and CD8(+) T cells, Int. Rev. Immunol. 35 (6) (2016) 477–488, https://doi.org/10.3109/08830185.2015.1082178.
[45] S. Le, H. Zhang, X. Huang, S. Chen, J. Wu, S. Chen, X. Ding, S. Chen, J. Zhao, H. Xu, J. Cui, Y. Zou, J. Yu, L. Jiang, J. Wu, P. Ye, J. Xia, PKM2 activator TEPP-46 attenuates thoracic aortic aneurysm and dissection by inhibiting NLRP3 inflammasome-mediated IL-1beta secretion, J. Cardiovasc. Pharmacol. Therapeut. 25 (4) (2020) 364–376, https://doi.org/10.1177/1074248420919966.
[46] J.D. Hutcheson, E. Aikawa, Extracellular vesicles in cardiovascular homeostasis and disease, Curr. Opin. Cardiol. 33 (3) (2018) 290–297, https://doi.org/10.1097/HCO.0000000000000510.
[47] R. Martinez-Pinna, A.G. de Peredo, B. Monsarrat, O. Burlet-Schiltz, J.L. Martin-Ventura, Label-free quantitative proteomic analysis of human plasma-derived microvesicles to find protein signatures of abdominal aortic aneurysms, Proteonomics Clin. Appl. 8 (7–8) (2014) 620–625, https://doi.org/10.1002/prca.201400010.
[48] S.L. Lu, G.H. Dang, J.C. Deng, H.Y. Liu, B. Liu, J. Yang, X.L. Ma, Y.T. Miao, C. T. Jiang, Q.B. Xu, X. Wang, J. Feng, Shikonin attenuates hyperhomocysteinemia-induced CD4(+) T cell inflammatory activation and atherosclerosis in ApoE(-/-) mice by metabolic suppression, Acta Pharmacol. Sin. 41 (1) (2020) 47–55, https://doi.org/10.1038/s41401-019-0308-7.
[49] J. Raffort, F. Lareyre, M. Clement, R. Hassen-Khodja, G. Chinetti, Z. Mallat, Monocytes and macrophages in abdominal aortic aneurysm, Nat. Rev. Cardiol. 14 (8) (2017) 457–471, https://doi.org/10.1038/nrcardio.2017.52.
[50] M.L. McCormick, D. Gavrila, N.L. Weintraub, Role of oxidative stress in the pathogenesis of abdominal aortic aneurysms, Arterioscler. Thromb. Vasc. Biol. 27 (3) (2007) 461–469, https://doi.org/10.1161/01.ATV.0000257552.94483.14.
[51] C. Koksal, M. Ercan, A.K. Bozkurt, T. Cortelekoglu, D. Konukoglu, Abdominal aortic aneurysm or aortic occlusive disease: role of trace element imbalance, Angiology 58 (2) (2007) 191–195, https://doi.org/10.1177/0003319707300354.
[52] Y. Zhao, Y. Li, R. Zhang, F. Wang, T. Wang, Y. Jiao, The role of erastin in ferroptosis and its prospects in cancer therapy, OncoTargets Ther. 13 (2020) 5429–5441, https://doi.org/10.2147/OTT.S254995.
[53] Z. Gao, G. Deng, Y. Li, H. Huang, X. Sun, H. Shi, X. Yao, L. Gao, Y. Ju, M. Luo, Actinidia chinensis planch prevents proliferation and migration of gastric cancer associated with apoptosis, ferroptosis activation and mesenchymal phenotype suppression, Biomed. Pharmacother. 126 (2020) 110092, https://doi.org/10.1016/j.biopha.2020.110092.
[54] D. Lu, Z. Yang, Q. Xia, S. Gao, S. Sun, X. Luo, Z. Li, X. Zhang, X. Li, ACADSB regulates ferroptosis and affects the migration, invasion, and proliferation of colorectal cancer cells, Cell Biol. Int. 44 (11) (2020) 2334–2343, https://doi.org/10.1002/cbin.11443.
[55] R. Martinez-Pinna, J.S. Lindholt, J. Madrigal-Matute, L.M. Blanco-Colio, M. Esteban-Salan, M.M. Torres-Fonseca, T. Lefebvre, S. Delbosc, J. Laustsen, F. Driss, M. Vega de Ceniga, L. Gouya, G. Weiss, J. Egido, O. Meilhac, J.B. Michel, J. Martin-Ventura, From tissue iron retention to low systemic haemoglobin levels, new pathophysiological biomarkers of human abdominal aortic aneurysm, Thromb. Haemostasis 112 (1) (2014) 87–95, https://doi.org/10.1160/TH13-08-0721.
[56] L.A. Youssef, A. Rebbaa, S. Pampou, S.P. Weisberg, B.R. Stockwell, E.A. Hod, S. L. Spitalnik, Increased erythrophagocytosis induces ferroptosis in red pulp macrophages in a mouse model of transfusion, Blood 131 (23) (2018) 2581–2593, https://doi.org/10.1182/blood-2017-12-822619.
[57] A.M. Nixon, E. Neely, I.A. Simpson, J.R. Connor, The role of HFE genotype in macrophage phenotype, J. Neuroinflammation 15 (1) (2018) 30, https://doi.org/10.1186/s12974-018-1057-0.
[58] T. Hirschhorn, B.R. Stockwell, The development of the concept of ferroptosis, Free Radic. Biol. Med. 133 (2019) 130–143, https://doi.org/10.1016/j.freeradbiomed.2018.09.043.